

The Carnegie-Irvine Galaxy Survey. VIII. Demographics of Bulges along the Hubble Sequence

HUA GAO (高桦)^{1,2} LUIS C. HO,^{2,1} AARON J. BARTH,³ AND ZHAO-YU LI⁴

¹*Department of Astronomy, School of Physics, Peking University, Beijing 100871, China*

²*Kavli Institute for Astronomy and Astrophysics, Peking University, Beijing 100871, China*

³*Department of Physics and Astronomy, University of California at Irvine, 4129 Frederick Reines Hall, Irvine, CA 92697-4575, USA*

⁴*Department of Astronomy, Shanghai Jiao Tong University, Shanghai 200240, China*

ABSTRACT

We present multi-component decomposition of high-quality *R*-band images of 320 disk galaxies from the Carnegie-Irvine Galaxy Survey. In addition to bulges and disks, we successfully model nuclei, bars, disk breaks, nuclear/inner lenses, and inner rings. Our modeling strategy treats nuclear rings and nuclear bars as part of the bulge component, while other features such as spiral arms, outer lenses, and outer rings are omitted from the fits because they are not crucial for accurate bulge measurements. The error budget of bulge parameters includes the uncertainties from sky level measurements and model assumptions. Comparison with multi-component decomposition from the *Spitzer* Survey of Stellar Structure in Galaxies reveals broad agreement for the majority of the overlapping galaxies, but for a considerable fraction of galaxies there are significant differences in bulge parameters caused by different strategies in model construction. We confirm that on average bulge prominence decreases from early to late-type disk galaxies, although the large scatter of bulge-to-total ratios in each morphological bin limits the application of Hubble type as an accurate predictor of bulge-to-total ratio. In contrast with previous studies claiming that barred galaxies host weaker bulges, we find that barred and unbarred spiral galaxies have similar bulge prominence.

Keywords: galaxies: bulges — galaxies: elliptical and lenticular, cD — galaxies: photometry — galaxies: spiral — galaxies: structure

1. INTRODUCTION

Motivated by the wealth of information stored in the morphological structures of galaxies, Ho et al. (2011) initiated the Carnegie-Irvine Galaxy Survey (CGS) to investigate the optical photometric properties of 605 bright galaxies in the southern hemisphere. Detailed analysis of the high-quality CGS images has yielded significant insights into many aspects of the Hubble sequence of galaxies, including the nature of disk breaks (Li et al. 2011), the formation history of ellipticals (Huang et al. 2013a,b, 2016), the bar buckling phenomenon (Li et al. 2017), the nature of S0s (Gao et al. 2018), and the origin of spiral arms (Yu & Ho 2018a,b). Galaxy bulges are, of course, one of the fundamental, defining characteristics of the Hubble sequence, and hence constitute a central theme of this long-term program.

As ellipticals and bulges bear resemblance in many aspects of their observational properties (e.g., Faber 1977; Gott 1977; Renzini 1999), they were once thought to have similar origin: both form out of rapid, violent processes, such as gravitational collapse (Eggen et al. 1962)

and mergers (Toomre 1977; Bournaud 2016). However, in recent decades, there has been increasing appreciation that bulges actually constitute a heterogeneous population. Bulges in late-type spirals show a younger stellar population, more flattened stellar light distribution, and more rotation-dominated kinematics compared with bulges in early-type disks (e.g., Wyse et al. 1997; Kormendy & Kennicutt 2004; Fisher & Drory 2008; Fisher et al. 2009; Laurikainen et al. 2016). These dichotomies in bulge properties suggest distinct formation physics. In addition to violent processes, secular evolution, facilitated by nonaxisymmetries in the galaxy potential, is able to transport gas with low angular momentum to galaxy centers to build up bulges that resembles disks rather than merger-built ellipticals (e.g., Kormendy & Kennicutt 2004; Athanassoula 2005; Sellwood 2014; Tonini et al. 2016). The disky bulges formed in this manner are commonly referred to in the literature as pseudobulges, to distinguish them from classical bulges.

Despite the importance of bulges in defining the Hubble sequence and their rich formation physics, robust

quantitative measurements of their structural parameters are yet to be achieved for large, well-defined samples. One-dimensional (1D) fitting of galaxy surface brightness profiles (e.g., Kormendy 1977a,b; Burstein 1979) and two-dimensional (2D) fitting of galaxy images (e.g., Shaw & Gilmore 1989; Byun & Freeman 1995; de Jong 1996a) are the two widely employed parametric techniques. Non-parametric techniques are less often used because of the difficulty of applying them to nearly face-on cases (e.g., Kent 1986; Capaccioli et al. 1987; Scorza & Bender 1990; Simien & Michard 1990). In terms of parametric fitting, 2D methods are superior because they preserve the maximum amount of spatial information on morphologically distinct components and because they conserve flux during the convolution process (Byun & Freeman 1995; de Jong 1996a; see Section 1 of Gao & Ho 2017 for a review of the methods). Nevertheless, both 1D and 2D methods suffer from the uncertainties introduced by the non-uniqueness of input surface brightness models.

In order to clarify which morphological features are most essential in 2D model construction when the primary intent is to obtain robust bulge parameters, Gao & Ho (2017) selected a representative sample from CGS that covers a sufficiently wide range of morphological features (bars, lenses, rings, and spiral arms) and explored the impact of modeling the secondary morphological features. They showed that modeling nuclear and inner lenses/rings and disk breaks has considerable impact on bulge parameters, whereas outer lenses/rings and spiral arms have a negligible effect. For example, failure to model disk breaks or lenses introduces errors that can be as large as $\sim 50\%$ in bulge-to-total ratio (B/T) for barred galaxies (see also Kim et al. 2014). This important effect is generally ignored in many decomposition studies (e.g., Simard et al. 2011; Meert et al. 2015; Salo et al. 2015; but see Laurikainen et al. 2005; Kim et al. 2016; Méndez-Abreu et al. 2017). These alarming uncertainties compel us to measure a new set of bulge parameters for nearby galaxies, derived in a consistent manner following the optimal strategy defined in Gao & Ho (2017).

Toward this end, Gao et al. (2018) successfully decomposed 62 CGS S0 galaxies. This paper extends our previous work and presents a comprehensive catalog of bulge parameters for 320 non-edge-on disk galaxies in CGS. Definition of the sample and description of the data are given in Section 2. We closely follow and expand the strategy in Gao & Ho (2017) to decompose the galaxies, as detailed in Section 3. We compare the CGS bulge parameters with those from the *Spitzer* Survey of Stellar Structure in Galaxies (S⁴G; Sheth et al. 2010) in

Section 4. In Section 5, we study how B/T is distributed along the Hubble Sequence. Section 6 summarizes the paper.

2. SAMPLE AND DATA

The CGS sample is defined by $B_T \leq 12.9$ mag and $\delta < 0^\circ$, without any reference to morphology, size, or environment. Details of the observations and data reduction are given in Ho et al. (2011) and Li et al. (2011), and will not be repeated here. We focus on the images taken in the R band because this filter is less sensitive to dust extinction and young stars; we avoid the I band because its point-spread function (PSF) suffers from the “red halo” effect (see Appendix A of Huang et al. 2013a). The majority of the R -band images are of high quality: the median seeing is $1''.01$, the median surface brightness depth is 26.4 mag arcsec⁻², and the field-of-view of $8'.9 \times 8'.9$ is large enough to ensure robust sky determination for most of the galaxies.

The sample analyzed in this paper is an extension to the sample of S0s presented in Gao et al. (2018). We add 304 non-edge-on spirals selected with morphological type index $0 < T \leq 9.5$ and inclination angle $i \leq 70^\circ$. During the course of performing the decomposition, we ended up removing 46 galaxies for a variety of reasons: two galaxies do not have R -band images; one galaxy is edge-on with a razor-thin disk; two galaxies do not have photometric calibration; two galaxies are highly dust-attenuated and are located in fields extremely crowded with stars; ten galaxies are highly irregular; three galaxies do not yield reasonable fits; and 26 galaxies are bulgeless. This leaves 258 spirals with measurable bulges, which, when combined with the 62 S0s, results in a final sample of 320 disk galaxies. The bulgeless galaxies are of particular interest (e.g., Kormendy et al. 2010; Fisher & Drory 2011), but they are beyond the scope of this paper. We list them in Appendix A for future consideration. A brief description of the main morphological features of each successfully decomposed galaxy is given in Appendix B.

Figure 1 summarizes the basic parameters of the successfully decomposed sample of 320 galaxies. The stellar masses (M_\star) for 313 galaxies were derived from the total K_s magnitudes compiled in Ho et al. (2011) and mass-to-light ratios following Equation (9) in Kormendy & Ho (2013):

$$\log (M/L)_{K_s} = 1.055(B - V) - 0.9402, \quad (1)$$

using $(B - V)$ colors from CGS (Li et al. 2011). The galaxies in the sample are nearby (median $D_L = 26.1$ Mpc) and massive [median $\log (M_\star/M_\odot) = 10.57$]. Note that some of the S0s have morphological type

indices $T < -3$ due to the inclusion of misclassified ellipticals (Gao et al. 2018). The sample is dominated by intermediate-type spirals (Sb–Scd). When divided into three subsamples according to the presence of a bar or lens, we find that the lens galaxies are exclusively S0s and early-type spirals. They are, on average, the reddest and most massive galaxies in the sample. The barred galaxy sample is offset to slightly earlier Hubble types, redder colors, and higher masses compared with the unbarred objects.

3. METHODOLOGY

3.1. Preparation for Image Fitting

Following Gao & Ho (2017), we use the latest version (3.0.5) of GALFIT¹ (Peng et al. 2002, 2010) to perform 2D multi-component decompositions of the CGS disk galaxies. GALFIT is a highly flexible and fast image-fitting algorithm that uses the Levenberg-Marquardt technique to find the optimum solution. It provides many analytic functions to represent the radial surface brightness profiles of objects/components of interest, including the widely used Sérsic (1968), exponential, and modified Ferrer profile. The profiles are projected onto the image plane via ellipses, or more complicated azimuthal functions such as Fourier modes, coordinate rotation, and bending modes to break from axisymmetry, for the purpose of producing realistic-looking galaxies. Furthermore, each component can be truncated at a given radius and at a given rate. In practice, however, we only make use of a limited set of its features, as described in Section 3.2.

For each run, GALFIT requires a data image, a PSF image, a mask image, and an input surface brightness model of the galaxy. The data images, PSF images, and mask images were prepared in Ho et al. (2011). We do not subtract the sky from the images before fitting, because we aim to solve the sky level simultaneously during the fit, which has proven to be feasible (see Appendix B.2 of Gao & Ho 2017). We modify the mask image to account for central dust lanes that are prevalent in late-type spirals (see notes in Appendix B). Identification of the major dust lanes is based on $B-R$ color maps. We allow sigma (noise) images to be internally generated by GALFIT. The convolution box diameter is set to 40–80 times the seeing disk, as suggested on the GALFIT website². As mentioned in the Introduction, the uncertainties in bulge parameters introduced by non-unique

models are significant, especially for CGS galaxies that are so bright and well-resolved that the effects of signal-to-noise ratio and resolution are marginal. Therefore, an adequate input model is crucial for deriving accurate bulge parameters. The strategy of preparing models will be detailed in Section 3.2.

As the CGS galaxies are bright and well-resolved, the best-fit parameters do not depend sensitively on their inputs, as long as we provide reasonable initial guesses. The only exception are the break radius and softening length when fitting broken disks, but these do not carry much physical significance, and they are often fixed to reasonable values. Some of the initial guesses are obtained from Ho et al. (2011), including galaxy centroid, disk ellipticity, and disk position angle. Other initial parameters, such as surface brightness, profile shape, ellipticity, and size of bulge, bar, and lens, are estimated through manual inspection of the image and its isophotal analysis. We identify the radial range where the component dominates the total light and visually examine the image and the profiles of surface brightness, ellipticity, and position angle to estimate their corresponding initial parameters. The initial guess for break radius is estimated by manual inspection of the surface brightness profile.

3.2. Model Construction

Based on the lessons learned from our detailed study of 2D decomposition methods (Gao & Ho 2017), we are aware of which parts of the galaxy should be modeled or can be omitted, and of the penalties for ignoring certain parts of the galaxy in the model. Therefore, we prepare just a *single* model for each galaxy, based on identification of its morphological features through detailed inspection of the images, color maps, structure maps, and isophotal analysis products from Ho et al. (2011) and Li et al. (2011). Specifically, we recognize a bulge as extra light above the inward extrapolation of the disk. We identify a strong bar according to its peak in the ellipticity profile and its roughly constant position angles at the radial range where its light dominates; the images, color maps, and structure maps provide extremely useful additional diagnostics when a bar is weak or viewed end-on. A lens can be recognized as a shelf on the surface brightness profile, featuring a sharp decline in surface brightness in its outskirts. Spiral arms and rings are readily identified by visual examination of the images, color maps, and structure maps. In addition to bulges and disks, we model bars, disk breaks, nuclear and inner lenses, and inner rings, but do not treat nuclear rings or bars separately because we consider them as part of the bulge. As with Gao et al. (2018), we model nuclear point

¹ <https://users.obs.carnegiescience.edu/peng/work/galfit/galfit.html>

² <https://users.obs.carnegiescience.edu/peng/work/galfit/TFAQ.html>

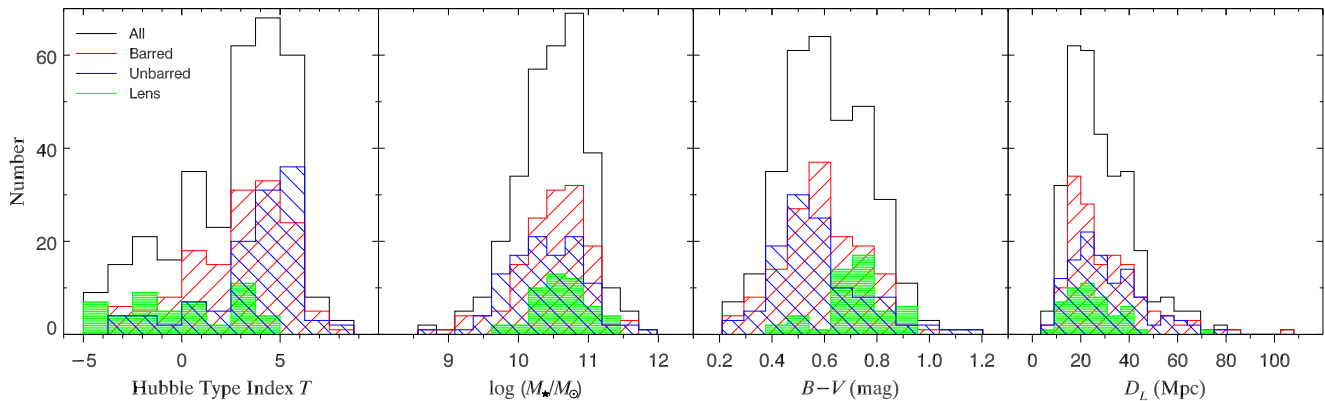


Figure 1. Basic properties of the sample. From left to right, distribution of morphological type index T , stellar mass, optical color $B-V$, and luminosity distance (D_L). The solid histograms represent the successfully decomposed galaxies that are divided into three subsamples: barred (red), unbarred (blue), and unbarred galaxies but have a lens (hereafter lens galaxies; green). Data from Ho et al. (2011) and Li et al. (2011).

sources (hereinafter nuclei) when present; they can be identified as abrupt changes in the central color profile. Spiral arms and outer lenses/rings have been shown to be not crucial for measuring accurate bulge parameters, and thus will not be treated. Unless specifically noted in Appendix B, we follow the above rules to construct surface brightness models for all the galaxies. The best-fit models of 320 CGS disk galaxies are shown in Figure 2, and the best-fit parameters are summarized in Table 1.

Although GALFIT is a feature-rich tool, only part of its functionality is needed to model the aforementioned features. Here we only provide necessary details of the adopted radial profiles and azimuthal functions and refer readers to Peng et al. (2010) and Section 3.2 of Gao & Ho (2017) for detailed descriptions and illustrations of them. The nucleus is represented by the user-provided PSF and therefore does not have an analytic functional form (see Figure 3 for an example). Following common practice, we model the radial profile of the bulge using the Sérsic function,

$$\Sigma(r) = \Sigma_e \exp \left[-\kappa \left(\left(\frac{r}{r_e} \right)^{1/n} - 1 \right) \right], \quad (2)$$

where r_e is the effective radius, Σ_e is the surface brightness at r_e , and n is the Sérsic index; κ is related to n by the incomplete gamma function, $\Gamma(2n) = 2\gamma(2n, \kappa)$ (Ciotti 1991). We also use the Sérsic function, usually with $n < 1$, to represent lenses or ovals³ (Figure 4), or disk subcomponents that have shallow light profiles (Figure 5). When $n = 1$, the Sérsic function is simply

the exponential profile of a disk,

$$\Sigma(r) = \Sigma_0 \exp \left(-\frac{r}{r_s} \right), \quad (3)$$

where Σ_0 and r_s are the central surface brightness and scale length, respectively. Figure 6 illustrates the simplest model configuration in our study: Sérsic bulge+exponential disk. When the exponential profile does not describe the disk component well, for instance when disk breaks, lenses, or rings are present, it can be substituted by a more general Sérsic profile (e.g., Figure 3). If a single function does not suffice, we use a combination of profiles to represent the disk. For instance, a combination of two truncated exponential functions with the same orientation and ellipticity can be used to model Type II (Figure 2) and Type III (Figure 7) disks⁴. A combination of functions of different types with possibly different orientations and ellipticities can be used to model photometrically distinct disk subcomponents, including extra disks (Figure 5) and lenses (Figure 4). Bars are described by the modified Ferrer profile (e.g., Figure 2; Binney & Tremaine 1987),

$$\Sigma(r) = \Sigma_0 \left[1 - (r/r_{\text{out}})^{2-\beta} \right]^\alpha, \quad (4)$$

where Σ_0 is the central surface brightness, α governs the sharpness of the outer truncation, β describes the central flatness of the profile, and r_{out} is the radius where the profile drops to 0 and remains 0 beyond it. We generally follow Gao & Ho (2017) and let α and β free unless they go over the allowed range $0 \leq \alpha \leq 5$. To be conservative,

³ We do not distinguish between lenses and ovals in disk galaxies.

⁴ The Type II (down-bending) and Type III (up-bending) disks have surface brightness profiles deviating from the exponential profile (Type I; e.g., Freeman 1970; Erwin et al. 2005, 2008; Pohlen & Trujillo 2006).

we fix α to 2 and β to 0 for weak bars. We fit the sky background simultaneously with the galaxy. The sky, represented by a first-order bivariate polynomial, is

$$\Sigma_{\text{sky}}(x, y) = \Sigma_{\text{sky}}(x_c, y_c) + (x - x_c) \frac{d\Sigma_{\text{sky}}}{dx} + (y - y_c) \frac{d\Sigma_{\text{sky}}}{dy}, \quad (5)$$

where (x_c, y_c) is the geometric center of the image and $d\Sigma_{\text{sky}}/dx$ and $d\Sigma_{\text{sky}}/dy$ are the sky flux gradients along each dimension of the image. To be cautious, for galaxies that are angularly large we fix the sky component to the sky level measured via the direct approach described in Appendix B.1 of Gao & Ho (2017).

The default azimuthal shape of each galaxy component is an ellipse,

$$r(x, y) = \left[(x - x_0)^2 + \left(\frac{y - y_0}{q} \right)^2 \right]^{1/2}, \quad (6)$$

where (x_0, y_0) is the centroid of the ellipse, the x -axis is aligned with the major axis of the ellipse, and q is the axis ratio. The Fourier modes perturb the ellipse in a way described by

$$r(x, y) = r_0(x, y) \left(1 + \sum_{m=1}^N a_m \cos[m(\theta + \phi_m)] \right), \quad (7)$$

where r_0 is the unperturbed radius, a_m is the amplitude for mode m , $\theta = \arctan((y - y_0)/((x - x_0)q))$, and ϕ_m is the phase angle relative to θ . The Fourier modes are generally not invoked, except for cases that need to model boxy/peanut bulges ($m = 4$; Figure 2) or lopsided disks ($m = 1$). Alternatively, the bending modes can induce curvature by only perturbing the y -axis following

$$y' = y + \sum_{m=1}^N a_m \left(\frac{x}{r_{\text{scale}}} \right)^m, \quad (8)$$

where a_m is similar to the one in Fourier modes and r_{scale} is the scale radius of the corresponding radial profile (e.g., r_e for Sérsic function and r_s for exponential function). Note that we apply the bending modes only once in this study, in order to model the twisted bar of IC 4618 ($m = 2$).

The truncation function can alter both the radial profile and azimuthal shape of components. We restrict its applications to create composite profiles to model disk breaks as well as rings (see Figures 2 and 7 for examples). Such a composite profile has an inner part described by a certain analytic function and an outer part that behaves as another, and they are modified by the same truncation function, albeit in opposite manners (outer truncation and inner truncation). In such

cases, the truncation function does not carry any physical meaning but only serves to link the inner and outer parts. Moreover, the overlap region of the two parts can naturally produce ring-like features. The truncation function is basically a hyperbolic tangent function, and its functional dependence on various parameters is given schematically by

$$P(x, y) = \tanh(x, y; x_0, y_0, r_{\text{break}}, \Delta r_{\text{soft}}, q, \theta_{\text{PA}}), \quad (9)$$

where (x_0, y_0) is the center, q is the axis ratio, and θ_{PA} is the position angle of the truncation function. These three parameters are hidden by default; if not specified, their values are inherited from the component that is modified by the truncation function. The break radius r_{break} marks the location where the flux of the truncated model drops to 99% of its original flux. The softening length Δr_{soft} is defined as $r_{\text{soft}} - r_{\text{break}}$ or $r_{\text{break}} - r_{\text{soft}}$ for outer truncation or inner truncation, respectively, where r_{soft} is the radius where the truncated model flux drops to 1% of its original flux. Its detailed analytic form is lengthy and is not of immediate interest; readers can consult Appendix B in Peng et al. (2010) for details. Components are modified by the truncation function by multiplying the original flux distribution with P for inner truncation and with $1 - P$ for outer truncation.

Fig. Set 2. Best-fit models of CGS disk galaxies.

3.3. Uncertainties of Bulge Parameters

As CGS galaxies are bright and well-resolved, the noise and PSF contribute negligibly to the uncertainties of the bulge parameters (total magnitude m , bulge-to-total ratio B/T , effective surface brightness μ_e , Sérsic index n , effective radius r_e , and ellipticity ϵ). The major source of uncertainty comes from sky level measurements and, more importantly, model assumptions. We measure the sky-induced uncertainties as variations of the best-fit bulge parameters when perturbing the sky levels around $\pm 1\sigma_{\text{sky}}$ of the best-fit sky levels, where uncertainties of the sky level σ_{sky} are measured as the root-mean-square of the residuals measured from randomly placed boxes in the sky-dominated region of the sky-subtracted data image (see Appendix B of Gao & Ho 2017 for details).

One source of systematic uncertainty comes from omission of certain features of the galaxy in the model. The effects were estimated by Gao & Ho (2017) by comparing bulge parameters from input models with and without the features. We repeat their conclusions here. Ignoring outer lenses/rings will induce uncertainties of 0.05 mag, 7.1%, 0.09 mag arcsec⁻², 5.8%, 5.3%, and 4.8% for m , B/T , μ_e , n , r_e , and ϵ , respectively. Spiral

Table 1. Best-fit Parameters and Bar/Lens Identifications of the Disk Galaxies

Name	m	B/T	μ_e	n	r_e	ϵ	D/T	b/T	Bar/Lens
	(mag)		(mag arcsec $^{-2}$)		(arcsec)				
(1)	(2)	(3)	(4)	(5)	(6)	(7)	(8)	(9)	(10)
ESO 027-G001	14.81 \pm 0.11	0.045 \pm 0.005	19.03 \pm 0.18	3.44 \pm 0.34	2.30 \pm 0.20	0.564 \pm 0.051	0.890	0.065	B
ESO 121-G026	14.00 \pm 0.11	0.091 \pm 0.008	18.68 \pm 0.16	1.58 \pm 0.13	2.54 \pm 0.20	0.214 \pm 0.018	0.825	0.084	B
ESO 137-G034	12.97 \pm 0.09	0.263 \pm 0.021	19.79 \pm 0.15	1.97 \pm 0.16	6.61 \pm 0.46	0.245 \pm 0.019	0.737	0.000	N
ESO 138-G010	13.56 \pm 0.35	0.066 \pm 0.017	21.64 \pm 0.63	2.14 \pm 0.68	11.60 \pm 4.46	0.252 \pm 0.005	0.930	0.000	N
ESO 186-G062	14.07 \pm 0.23	0.139 \pm 0.022	22.66 \pm 0.51	3.28 \pm 0.57	19.74 \pm 5.79	0.660 \pm 0.051	0.840	0.021	B
ESO 213-G011	13.90 \pm 0.17	0.085 \pm 0.012	21.34 \pm 0.28	2.36 \pm 0.30	8.71 \pm 1.34	0.293 \pm 0.023	0.915	0.000	N
ESO 221-G026	11.13 \pm 0.17	0.534 \pm 0.062	19.46 \pm 0.46	5.00 \pm 0.65	13.48 \pm 3.72	0.528 \pm 0.041	0.466	0.000	?
ESO 221-G032	15.50 \pm 0.17	0.029 \pm 0.004	18.44 \pm 0.28	2.35 \pm 0.30	1.03 \pm 0.16	0.202 \pm 0.016	0.971	0.000	N
ESO 269-G057	12.79 \pm 0.10	0.207 \pm 0.024	18.10 \pm 0.17	1.37 \pm 0.14	3.68 \pm 0.32	0.287 \pm 0.026	0.724	0.069	B
ESO 271-G010	16.41 \pm 0.10	0.014 \pm 0.001	21.54 \pm 0.15	1.48 \pm 0.12	4.36 \pm 0.31	0.586 \pm 0.045	0.948	0.038	W
ESO 320-G026	14.51 \pm 0.17	0.070 \pm 0.009	17.96 \pm 0.28	0.98 \pm 0.13	1.97 \pm 0.30	0.478 \pm 0.037	0.930	0.000	N
ESO 321-G025	16.83 \pm 0.10	0.012 \pm 0.001	19.76 \pm 0.15	0.57 \pm 0.05	2.37 \pm 0.17	0.720 \pm 0.056	0.954	0.034	W
ESO 380-G001	13.98 \pm 0.11	0.081 \pm 0.008	19.57 \pm 0.18	3.94 \pm 0.39	3.71 \pm 0.33	0.446 \pm 0.041	0.741	0.178	B
ESO 380-G006	12.23 \pm 0.13	0.284 \pm 0.032	20.52 \pm 0.21	2.86 \pm 0.30	12.33 \pm 1.48	0.298 \pm 0.027	0.716	0.000	L

NOTE—Col. (1): Galaxy name. Cols. (2)–(7): Total R -band magnitude of the bulge, bulge-to-total flux ratio, bulge surface brightness at the effective radius, bulge Sérsic index, bulge effective radius, and bulge ellipticity. Col. (8): Disk-to-total ratio. Col. (9): Bar-to-total ratio. Col. (10): Flag for the presence or absence of a bar/lens: B = definitely barred; W = weakly barred; N = no bar or lens; L = no bar but lens present; ? = uncertain.

(Table 1 is published in its entirety in machine-readable format. A portion is shown here for guidance regarding its form and content.)

arms in barred and unbarred galaxies impact bulge parameters in different manners, since spiral arms usually stop at the ends of the bar in barred galaxies, whereas they extend to the center in unbarred systems. Not including spiral arms in the model introduces uncertainties at the level of 0.14 mag, 11.7%, 0.24 mag arcsec $^{-2}$, 10.1%, 13.6%, and 0.4% for m , B/T , μ_e , n , r_e , and ϵ , respectively, for the bulges of unbarred galaxies; for barred galaxies, the corresponding values are 0.03 mag, 2.2%, 0.03 mag arcsec $^{-2}$, 1.1%, 1.4% and 0.4% for m , B/T , μ_e , n , r_e , and ϵ , respectively. Another source of systematic uncertainty stems from the use of different mathematical representations of the same disk surface brightness, which arises when we model disk breaks, lenses, and rings, along with the underlying disk. The typical contribution to the error budget is 0.09 mag, 6.7%, 0.15 mag arcsec $^{-2}$, 8.0%, 6.9%, and 7.7% for m , B/T , μ_e , n , r_e , and ϵ , respectively. The final uncertainties of the bulge parameters in Table 1 represent the quadrature sum of the uncertainties from these various considerations.

4. COMPARISON WITH S⁴G

Some of the CGS galaxies were also observed as part of S⁴G. Salo et al. (2015) applied GALFIT to perform human-supervised, multi-component decomposition of the 3.6 μ m images. In addition to bulges and disks, they fit bars and nuclear point sources, with up to four components in the model.

Although their philosophy in construction of multi-component models is similar to ours, the details differ greatly. For instance, they do not treat disk breaks, and we do not limit our fits to a pre-determined number of components, if more sophisticated models are deemed necessary for complex situations. It is of interest to know how our different approaches affect the final results. We cross match our sample with the S⁴G sample and find 101 galaxies in common that have bulge decompositions of relatively high quality (at least 4 according to the rating system of Salo et al. 2015; see their Section 5.1). Figure 8 compares the effective radii, apparent ellipticities, bulge-to-total ratios, and Sérsic indices from the two independent sets of decompositions. We find broad consistency between our results and those of the S⁴G Pipeline4: 74%, 74%, 68%, and 90% of the bulge parameters B/T , n , r_e , and ϵ , respectively, agree with each other within a factor of 2. But we also find many cases of S⁴G-derived bulge parameters (especially B/T , r_e , and n) that are systematically lower than our values for barred galaxies. We suspect that this is due to the fact that disk breaks are prevalent in barred galaxies, and failure to model the disk breaks will underestimate the contribution from the bulge and bar (e.g., Gao & Ho 2017).

However, some of the extreme (larger than a factor of 2) outliers are disconcerting and require closer scrutiny. Upon careful examination, we find that almost all the extreme outliers can be attributed to systematic differ-

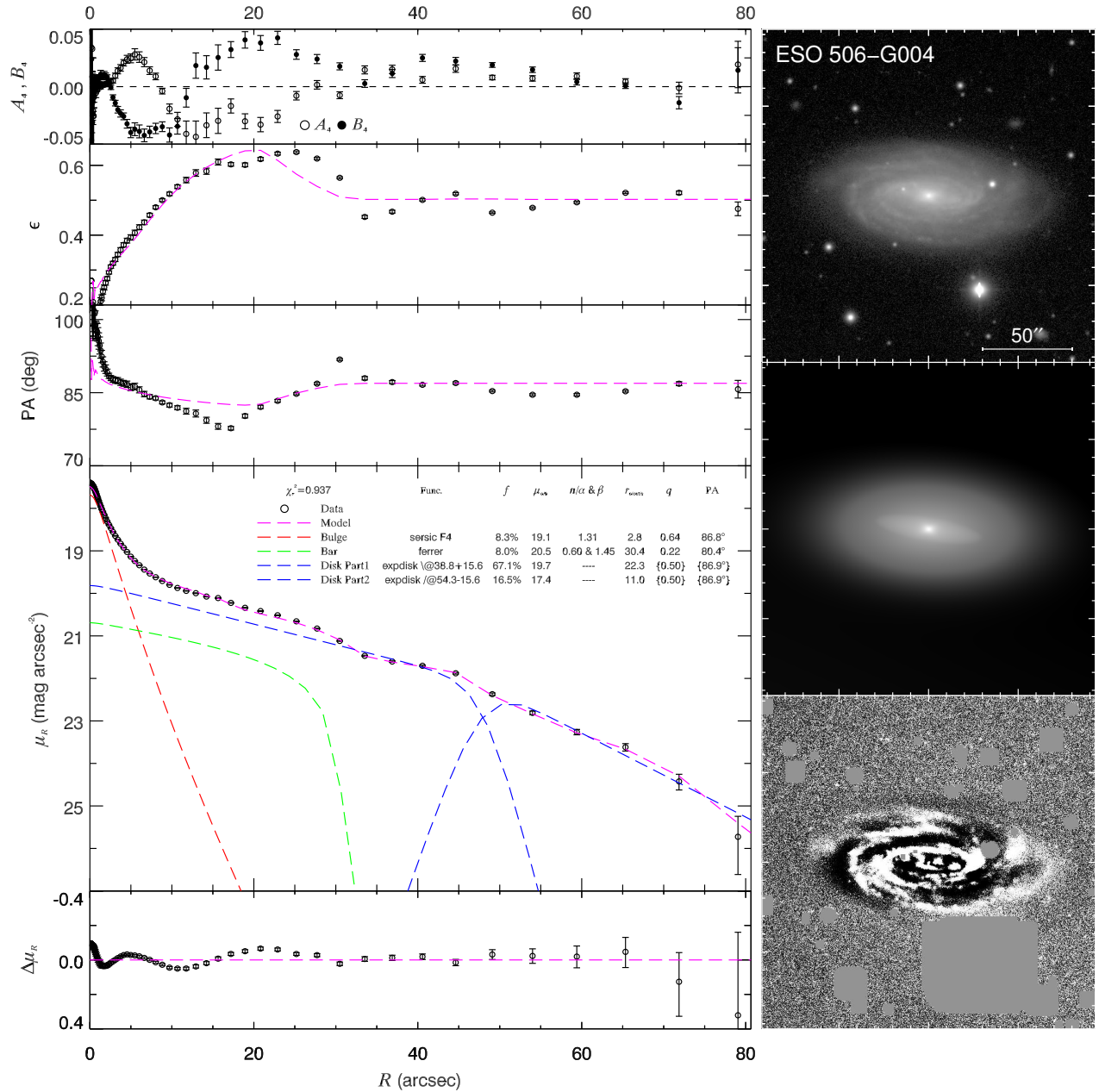


Figure 2. Best-fit model of ESO 506-G004. The left panels display the isophotal analysis of the 2D image fitting. From top to bottom, the panels show the radial profiles of the fourth harmonic deviations from an ellipse (A_4 and B_4), ellipticity (ϵ), position angle (PA), R -band surface brightness (μ_R), and fitting residuals ($\Delta\mu_R$). Profiles of the data, the model, and the individual components are encoded consistently with different symbols, line styles, and colors, as explained in the legends. The text to the right of the legends gives detailed information on each component; from left to right, the columns describe the radial profile functions (PSF, Sérsic, exponential, and modified Ferrer) and whether they are complete or truncated (blank for complete, “@ $r_{\text{break}} + \Delta r_{\text{soft}}$ ” for outer truncation, and “/ $@r_{\text{break}} - \Delta r_{\text{soft}}$ ” for inner truncation) and their azimuthal shapes (blank for pure ellipse and F_n for Fourier modes $m = n$), the light fractions, the characteristic surface brightness (effective surface brightness μ_e for the bulge and central surface brightness μ_0 for the others), the shape parameters of the radial profiles (Sérsic index n for the Sérsic function and α & β for the modified Ferrer function), the characteristic radii (effective radius r_e for the Sérsic function, outer boundary r_{out} for the modified Ferrer function, and scale length r_s for the exponential function), the axis ratios (q), and the position angles (PA). The parameters can be constrained to be the same (braces) and/or fixed (brackets). Note that the surface brightness profile of the model is generated by fixing the geometric parameters to those of the data surface brightness profile, and the surface brightness profiles of individual components are generated along their major axes; hence, the model surface brightness profile is not a simple summation of the profiles of the individual components. The right panels display, from top to bottom, the grayscale R -band image, the best-fit model image, and the residual image. The images are shown using the same logarithmic stretch for the data and model image, and histogram equalization stretch for the residual image. All images are cropped to have the same size of $1.5D_{25}$, with D_{25} the isophotal galaxy diameter at $\mu_B = 25$ mag arcsec $^{-2}$, and are centered on the galaxy centroid, with north up and east to the left. (The complete figure set for 320 galaxies is available in the online journal.)

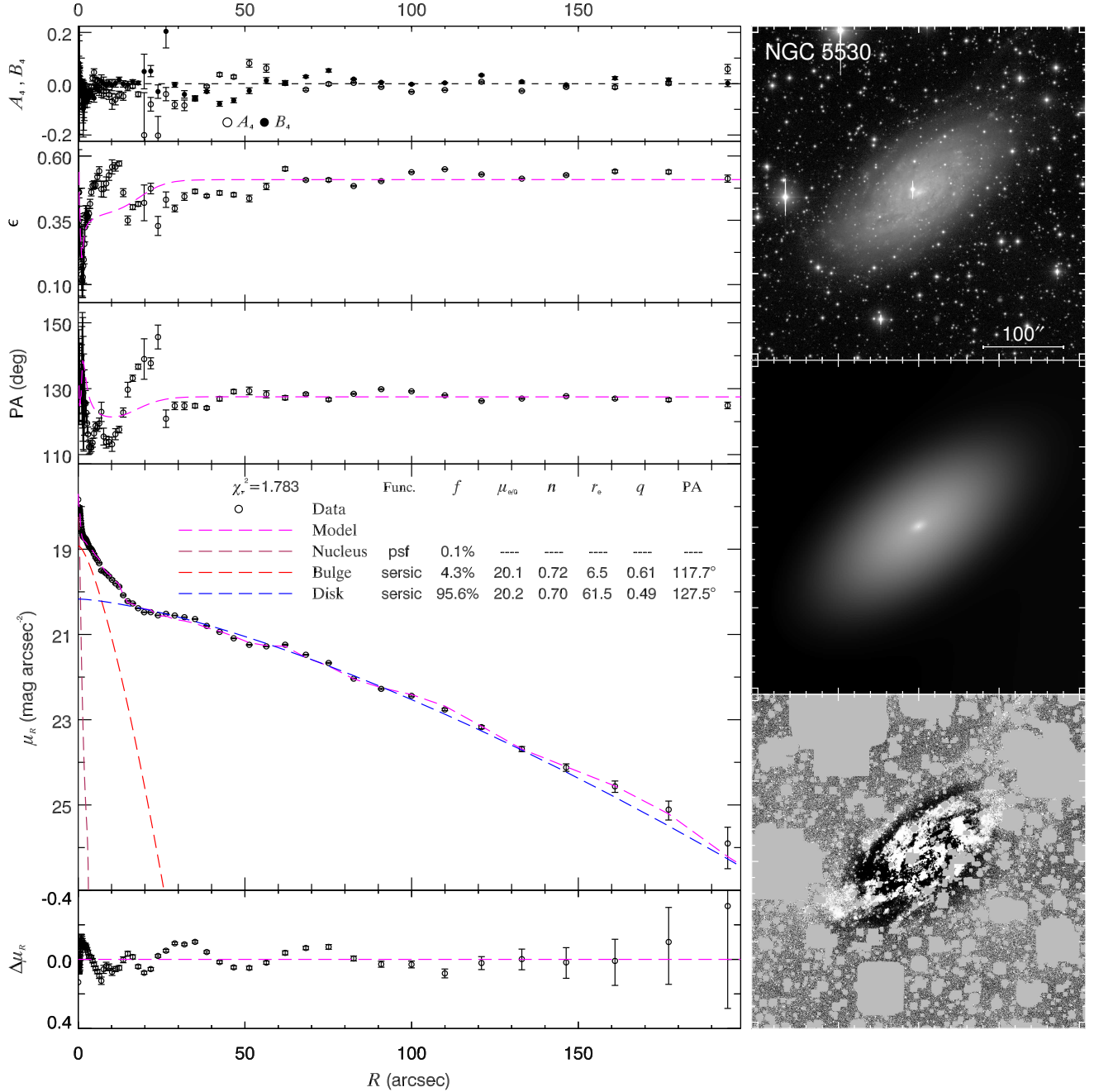


Figure 3. Best-fit model of NGC 5530, to illustrate how to model its nucleus and broken disk. Same convention as in Figure 2.

ences in model construction. Among the 15 extreme outliers with systematically lower values of B/T from S⁴G, 11 have disk breaks that were not treated⁵. The 11 extreme outliers with S⁴G B/T values larger than ours can be traced to various reasons, the most common

being the presence of a nucleus (not modeled by S⁴G), which leads to a systematic overestimation of the bulge Sérsic index (and bulge luminosity). Other reasons include the misidentification of disk galaxies as ellipticals and the neglect of extra disk components, such as thick disks and lenses. For instance, the three sources for which S⁴G derived $B/T = 1$ are, in fact, misclassified as ellipticals (Huang et al. 2013a), and we decomposed

⁵ They are IC 1993, IC 2051, NGC 1232, NGC 1292, NGC 1452, NGC 1640, NGC 3673, NGC 3887, NGC 4462, NGC 7513, and NGC 7590.

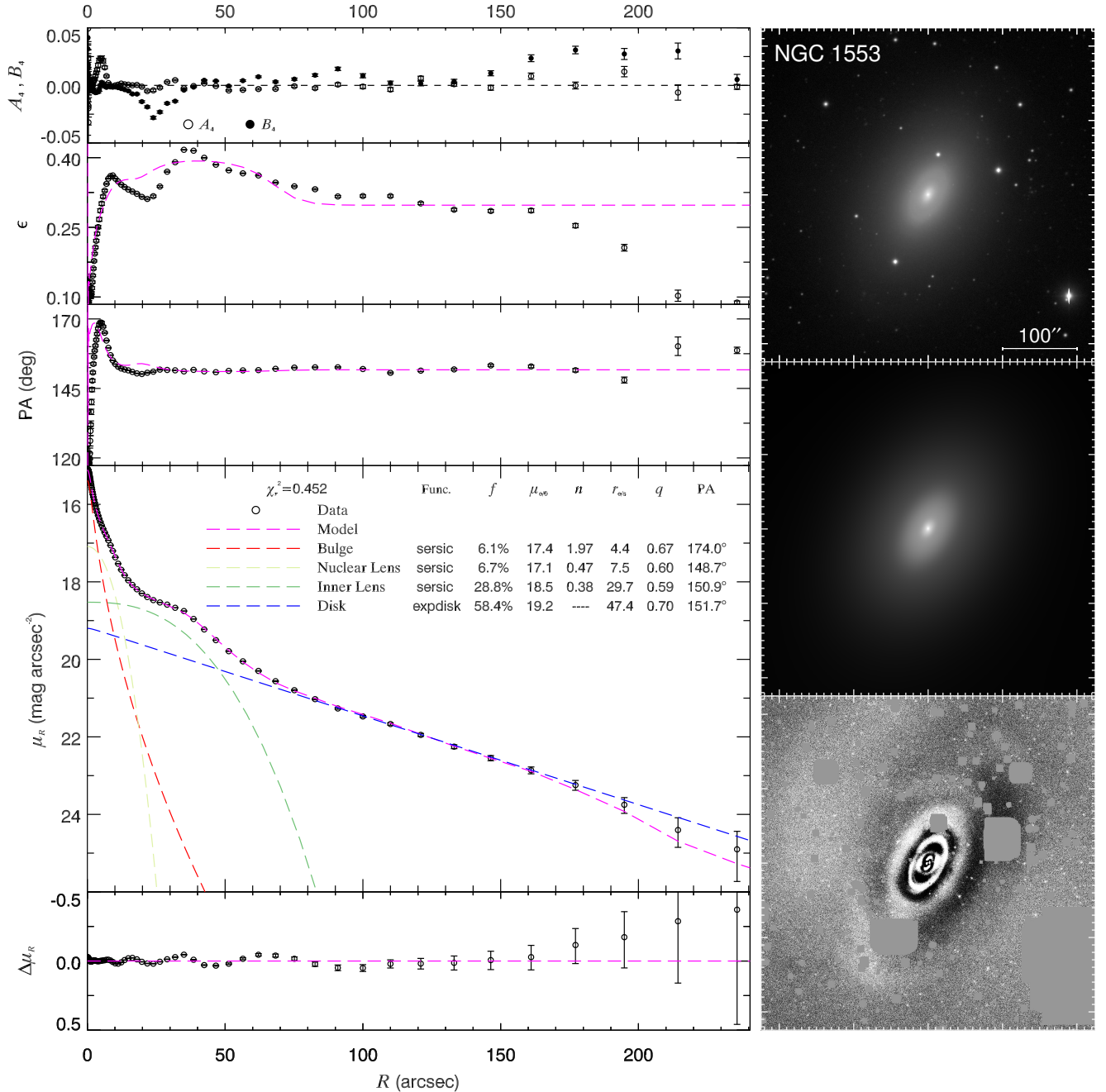


Figure 4. Best-fit model of NGC 1553, to illustrate how to model lenses. Same convention as in Figure 2.

them as S0s or spirals⁶. Among the 22 outliers with significantly smaller r_e derived from S⁴G, 15 are due to disk breaks that were not taken into account⁷. At the

⁶ IC 2006 and NGC 3904 are S0s with lenses, and NGC 7213 is a spiral galaxy that shows evident spiral and ring features in the central 30''.

⁷ They are IC 1953, IC 1993, IC 2051, NGC 1022, NGC 1084, NGC 1232, NGC 1292, NGC 1452, NGC 3673, NGC 3887, NGC 4462, NGC 4899, NGC 5339, NGC 7513, and NGC 7590.

same time, of the 10 sources with exceptionally large values of r_e from S⁴G, four are due to large-scale essential components that were missing in the model⁸ (e.g., bars, lenses, thick disks), three are actually S0s misclassified as ellipticals, as mentioned above, and two stem from neglecting a nucleus⁹. Among the 14 extreme outliers

⁸ They are NGC 584, NGC 1302, NGC 4050, and NGC 5078.

⁹ NGC 3892 and NGC 4802

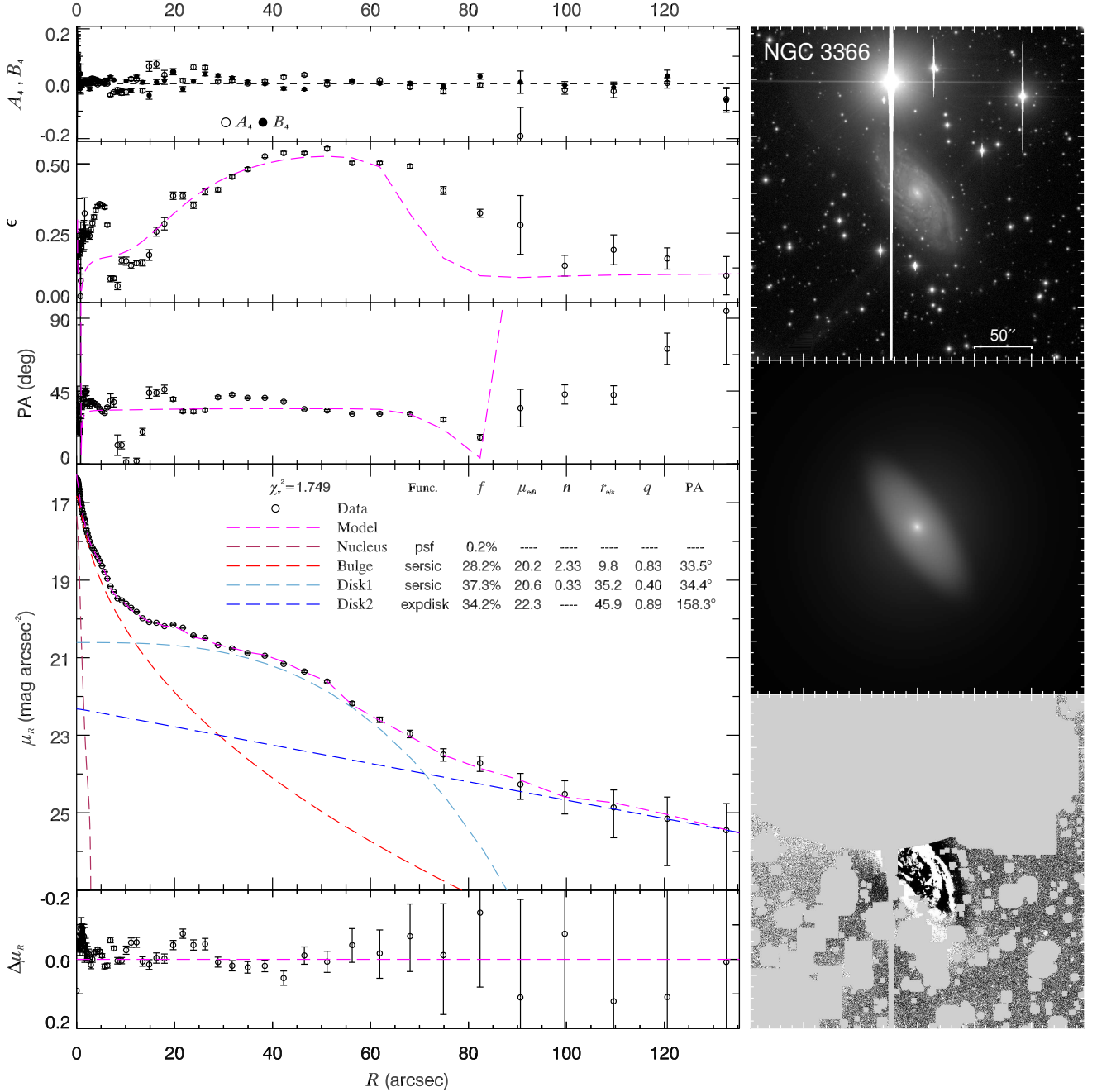


Figure 5. Best-fit model of NGC 3366, which has a two-disk configuration. Same convention as in Figure 2.

with lower S^4G values of n , nine are due to disk breaks¹⁰, and two are due to modeling lenses with an exponential instead of a low- n Sérsic function¹¹; of the 12 objects that are positive outliers in n , six are due to nuclei¹²,

¹⁰ They are IC 1993, IC 2051, NGC 1300, NGC 1640, NGC 3673, NGC 4462, NGC 7140, NGC 7590, and NGC 7755.

¹¹ NGC 1425 and NGC 3885

¹² They are NGC 150, NGC 4684, NGC 4802, NGC 4965, NGC 5339, and NGC 7531.

and four stem from large-scale essential components that are missing in model¹³ (e.g., bars, disks, and disk sub-components). In terms of ϵ , almost all of the extreme outliers are biased too high in S^4G . One-third of these cases are caused by missing components with high ellipticities near the bulge, such as bars, bar-like patterns produced by winding spiral arms, and additional disk

¹³ They are NGC 4050, NGC 5078, NGC 5468, and NGC 7213.

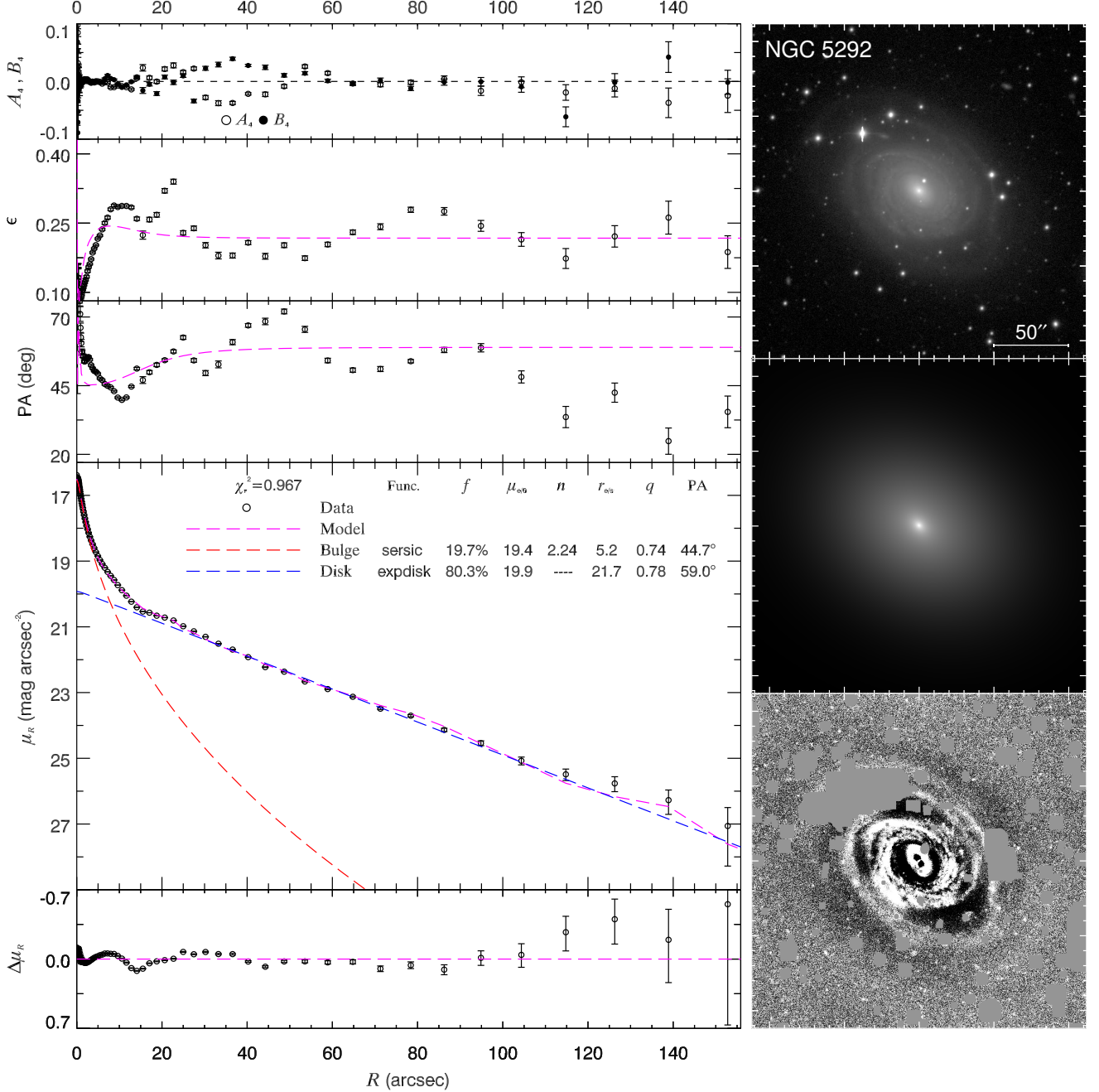


Figure 6. Best-fit model of NGC 5292, which has the simplest configuration of just a Sérsic bulge and an exponential disk. Same convention as in Figure 2.

components. Some are due to the effect of nuclei, which, when neglected, leads to larger n and r_e for the bulge and thus absorbs some of disk/bar light. Mistaking disks for ellipticals also results in larger ϵ (e.g., NGC 7213). The only single extreme outlier (NGC 4684) with a very low value of ϵ in S^4G is due to modeling its nucleus as the bulge.

To summarize: the above comparison re-emphasizes our motivation to provide a new set of revised bulge

parameters for nearby galaxies. Even though S^4G has already performed very careful, highly sophisticated multi-component decomposition, detailed comparison with our analysis reveals that significant discrepancies can still arise. The uncertainties of the bulge parameters are dominated entirely by systematic differences in model construction; wavelength effects play a minor role. As Gao & Ho (2017) stress, proper treatment of certain secondary morphological components are abso-

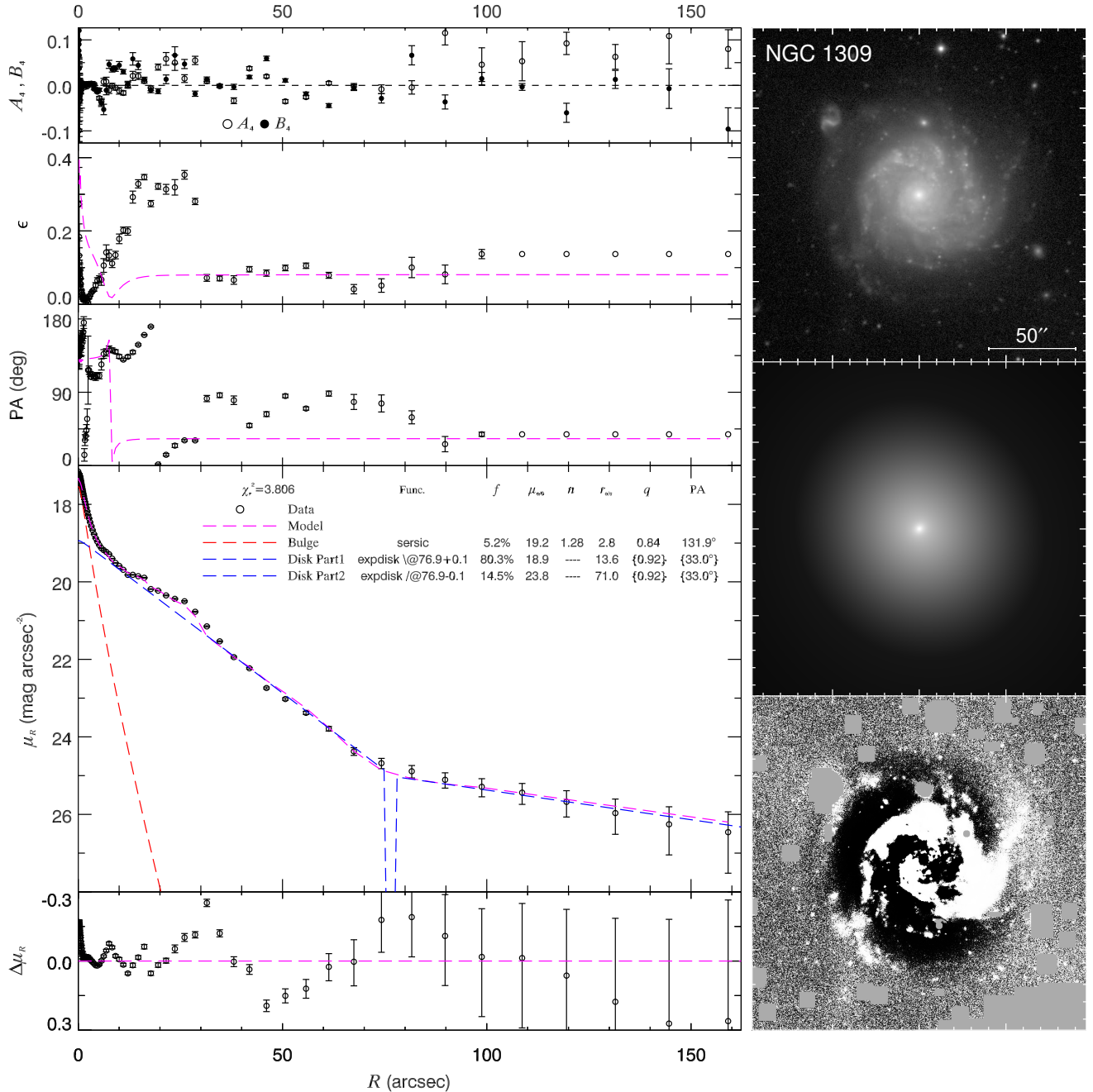


Figure 7. Best-fit model of NGC 1309, which has a Type III disk. Same convention as in Figure 2.

lutely indispensable—indeed, obligatory—if one wishes to obtain robust structural parameters for the bulge. The external comparison here further strengthens their conclusions.

5. BULGE PROMINENCE ALONG THE HUBBLE SEQUENCE

Bulge prominence is one of the key defining criteria of the Hubble classification scheme (Hubble 1926, 1936; Sandage 1961). Therefore, it is expected that

bulge properties should correlate with Hubble types to some extent. Huge effort has been devoted to investigate whether Hubble types are good predictors of bulge prominence and vice versa (e.g., Kent 1985; Kodaira et al. 1986; Simien & de Vaucouleurs 1986; Solanes et al. 1989). Many studies have shown that B/T does correlate with morphological type index T in an average sense, with minor counterarguments (Kodaira et al. 1986; Byun 1992; Grosbøl et al. 2004). However, previous studies were either limited by small sample size

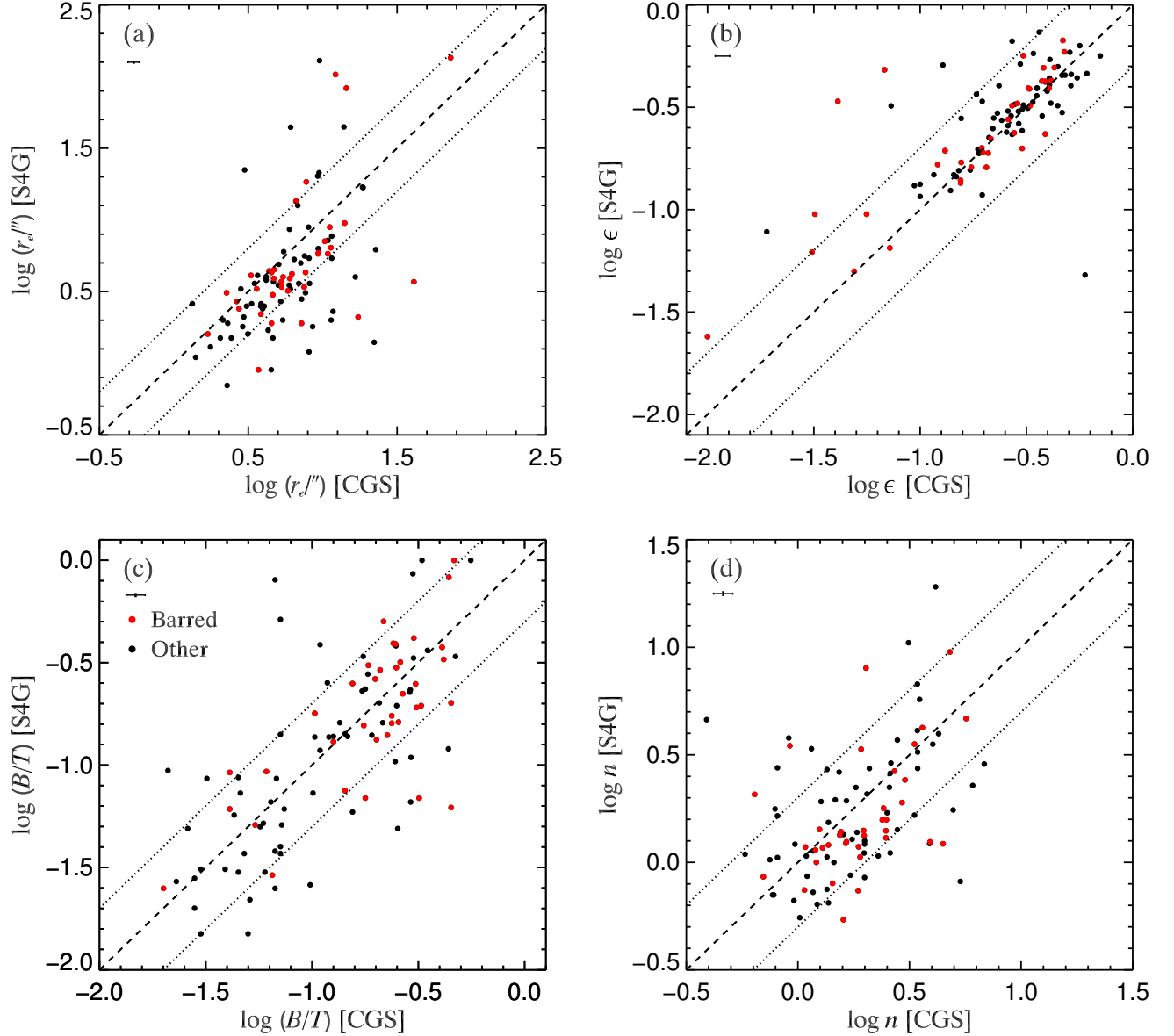


Figure 8. Comparison of CGS bulge parameters with S⁴G Pipeline4 results, for (a) effective radii, (b) apparent ellipticities, (c) bulge-to-total ratios, and (d) Sérsic indices. Barred galaxies are highlighted in red. Median errors of the bulge parameters are illustrated in the upper-left corner of each panel. The constant errors of S⁴G bulge parameters are median errors introduced by PSF and sky subtraction, as listed in Tables 3 and 4 of Salo et al. (2015). In each panel, the dashed line gives the one-to-one relation, and the dotted lines demarcate an offset of 0.3 dex (a factor of 2).

(e.g., Héraudeau & Simien 1995; de Jong 1996b; Khosroshahi et al. 2000; Graham 2001; Möllenhoff & Heidt 2001; Möllenhoff 2004), over-simplified decomposition techniques (e.g., Kent 1985; Simien & de Vaucouleurs 1986; Kodaira et al. 1986; Graham 2001), or incorrect assumptions of the bulge profile (e.g., Kent 1985; Simien & de Vaucouleurs 1986; Kodaira et al. 1986; Oohama et al. 2009). Subsequent efforts addressed some of these shortcomings (de Jong 1996b; Laurikainen et al. 2007, 2010; Weinzirl et al. 2009; Méndez-Abreu et al. 2017). This study represents a significant contribution toward

these efforts, with the employment of well-developed 2D techniques, more realistic model assumptions, and better understanding of the error budget. Using the vastly improved bulge measurements for a sizable sample presented in this paper, we revisit this classical problem and showcase the potential of our database.

Figure 9 shows the distribution of B/T in morphological bins from S0 to Sdm. We confirm previous findings that median B/T decreases toward late Hubble types. For individual galaxies, the Spearman’s rank correlation coefficient between B/T and morphological type index

T is -0.71 , and the correlation is statistically significant (p -value is 0.00). Excluding bins with fewer than 10 galaxies, the best-fit third-order polynomial to the mean B/T as a function of T is

$$\langle B/T \rangle = 0.29 \pm 0.01 - (0.042 \pm 0.006)T - (0.006 \pm 0.003)T^2 + (0.0011 \pm 0.0004)T^3. \quad (10)$$

The three bins of S0 galaxies have roughly constant B/T (see also Simien & de Vaucouleurs 1986; Khosroshahi et al. 2000; Laurikainen et al. 2007, 2010). Although the overall trend is similar to that of previous studies, it is worthwhile to note that many authors find that B/T systematically decreases for Hubble types later than $T = 4$ (e.g., Simien & de Vaucouleurs 1986; Héraudeau & Simien 1995; Graham & Worley 2008; Méndez-Abreu et al. 2017), but we do not¹⁴. We do not know whether this is genuine or a bias due to the selection of CGS galaxies against fainter galaxies in these late Hubble type bins. We confirm that most of the bins with meaningful statistics exhibit a large scatter in B/T (e.g., Kent 1985; Kodaira et al. 1986; Simien & de Vaucouleurs 1986; Weinzirl et al. 2009; Laurikainen et al. 2010). The scatter is especially remarkable among S0 galaxies, whose B/T can be as large as 0.7 and as small as those of Sc galaxies ($B/T \approx 0.1$; see also Gao et al. 2018). Other classification criteria in the Hubble sequence, such as properties of spiral arms, and classification errors may be responsible for the scatter present in all Hubble types. The large dispersion of bulge prominence at any given Hubble type precludes the use of Hubble type to quantitatively predict B/T .

Despite the general agreement of the systematic trend and scatter of B/T along the Hubble sequence, we note that studies that employ 1D techniques and classical models (i.e., a de Vaucouleurs bulge and an exponential disk) systematically overestimate B/T compared with our 2D multicomponent decomposition. For example, Simien & de Vaucouleurs (1986), Kent (1985), and Kodaira et al. (1986) measured optical $\langle B/T \rangle \gtrsim 0.5$ of S0s; Simien & de Vaucouleurs (1986) and Kent (1985) found no S0 with B/T smaller than ~ 0.3 . By contrast, we obtain $\langle B/T \rangle = 0.34 \pm 0.15$ in R -band. Less dramatic, though still significant, overestimates of bulge flux are also seen in later Hubble types. The de Vaucouleurs law ($n = 4$) has long been proven to be inadequate for most disk galaxies (see Figure 2b of Gao et al. 2018), especially those of late-type (Andredakis & Sanders 1994; Andredakis et al. 1995; de Jong 1996a). Application of

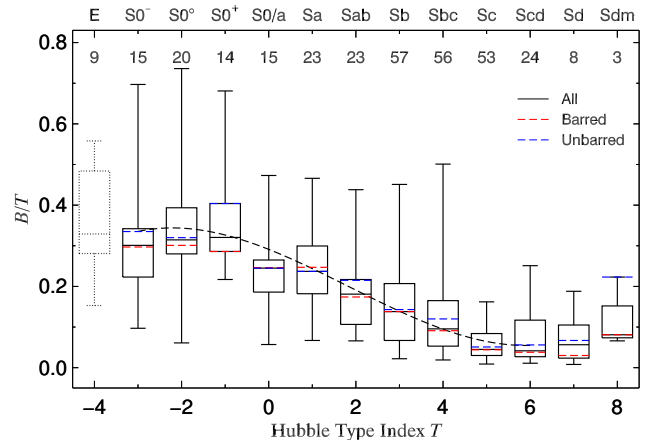


Figure 9. Distribution of B/T as a function of Hubble type. The morphological type index T is given in the bottom axis and the corresponding traditional Hubble types are given in the top axis. For each bin in morphological type, the distribution of B/T is described by a box-and-whisker plot, for which the box encloses the interquartile range and the whisker indicates its maximum and minimum. Note that we group all the S0s that were misclassified as ellipticals into the $T = -4$ bin (see Section 2) and distinguish them with the dotted box and whisker. The horizontal lines of each morphological bin represent the median for all galaxies (black), barred galaxies (red dashed), and unbarred galaxies (blue dashed). The dashed line represents the polynomial fit (Equation 10) to the mean B/T in Hubble type bins with more than 10 galaxies.

a universal de Vaucouleurs law to extract the bulges of all galaxy types will lead to systematic overestimates of the bulge flux (e.g., Oohama et al. 2009).

Finally, we divide the sample into barred and unbarred galaxies to examine their potential difference in bulge properties. Apart from S0s (see Section 4.1 of Gao et al. 2018), we find that the barred and unbarred galaxies have similar median B/T along the Hubble sequence, in contrast with some previous studies that show systematically weaker bulges in barred galaxies (e.g., Laurikainen et al. 2007; Weinzirl et al. 2009). We attribute the discrepancy to our more accurate decomposition that consistently accounts for disk breaks in barred galaxies, which, if neglected, leads to underestimation of the bulge flux.

6. SUMMARY

We perform 2D multi-component decompositions of 258 CGS spiral galaxies in R band. In addition to bulges and disks, we successfully model nuclei, bars, disk breaks, nuclear/inner lenses, and inner rings. Our decomposition intentionally ignores nuclear rings/bars, which we consider to be part of the photometric bulge,

¹⁴ For similar results, see Graham 2001; Grosbøl et al. 2004; Laurikainen et al. 2007, 2010; Weinzirl et al. 2009.

and we also do not treat spiral arms, outer lenses and outer rings because they are known to be unimportant for bulge measurements. We pay close attention to estimating robust errors for the derived bulge parameters, taking into account the uncertainties from sky level measurements and model assumptions. Together with the 62 CGS S0s separately analyzed by Gao et al. (2018), we present a homogeneous catalog of bulge parameters for 320 CGS disk galaxies. Comparison of our bulge parameters with the results from S⁴G shows significant discrepancies that cannot be accounted for by wavelength effects. We find that differences in model assumptions is the major source of the inconsistency, stressing the need to construct realistic models that consider all the necessary secondary morphological features in the image decomposition (Gao & Ho 2017).

We reevaluate the classic relation between bulge prominence and Hubble type, confirming that, while B/T decreases systematically from early to late-type disk galaxies, the scatter in B/T is considerable at any given morphological type. In contrast with previous

studies that claim barred galaxies host weaker bulges, we show that barred and unbarred galaxies have similar median B/T across the Hubble sequence except for S0s.

The catalog of bulge parameters presented here is a homogeneous and robust dataset, one that has the promise for new discoveries. Detailed analysis of the products, including statistics and correlation of bulge parameters, their scaling relations, and study of bulge types, will be presented in forthcoming papers.

This work was supported by the National Science Foundation of China (11721303) and the National Key R&D Program of China (2016YFA0400702). ZYL is supported by the Youth Innovation Promotion Association, Chinese Academy of Sciences. This research has made use of the NASA/IPAC Extragalactic Database (NED) which is operated by the Jet Propulsion Laboratory, California Institute of Technology, under contract with the National Aeronautics and Space Administration.

APPENDIX

A. THE BULGELESS GALAXIES

We tabulate the bulgeless galaxies and the presence of nuclei therein in Table 2.

B. NOTES ON INDIVIDUAL GALAXIES

ESO 027–G001: The galaxy is barred. We model its disk break at the edge of the spiral arms but ignore the disk break at $\sim 140''$, which is treated as an outer feature (e.g., outer lens and ring) when estimating bulge errors.

ESO 121–G026: We mask the dust lane on one side of the bar and model the disk break at the inner ring.

ESO 137–G034: There are many foreground stars, including two saturated ones near the bulge, that are carefully masked. We model the disk break at $\sim 40''$. The disk shows weak spiral arms. We mask the dust lane running through the bulge.

ESO 138–G010: There are many foreground stars. The nucleus is an NSC (Georgiev & Böker 2014). The disk shows diffuse spiral arms.

ESO 186–G062: The galaxy has a high- n bulge and a weak bar. We model its disk break at the edge of the spiral arms.

ESO 213–G011: We model the disk break at the edge of the spiral arms.

ESO 221–G026: The galaxy is classified as an elliptical in both HyperLeda (Paturel et al. 2003) and the Third Reference Catalog of Bright Galaxies (RC3; de Vaucouleurs et al. 1991), but Huang et al. (2013a) discovered some substructures in it. The galaxy is likely to be an edge-on system with a thin and a thick disk, which we provisionally model as a lens and a disk in our decomposition (see Figure 2.7). Its bar/lens identification is undecided (flagged as “?” in Table 1).

ESO 221–G032: The galaxy has a compact bulge. We model the gentle disk break at $\sim 20''$. The circumnuclear dust lanes are masked during the fitting.

ESO 269–G057: The galaxy has an end-on bar whose α and β are fixed. We model the disk break/lens at the bar radius. The dust lanes around the bulge are masked during the fitting.

ESO 271–G010: The galaxy has a weak bar whose α and β need to be fixed. We model the disk break at the edge of the spiral arms. A suspected weak nucleus is neglected.

ESO 320–G026: We model the disk break at the edge of the spiral arms.

ESO 321–G025: The galaxy has a highly flattened bulge. The bar parameters have to be fixed during the fitting. We model its disk break at the edge of the spiral arms.

Table 2. Basic Properties of the Bulgeless Galaxies

Name	T	$\log(M_*/M_\odot)$	Bar	Nucleus
(1)	(2)	(3)	(4)	(5)
ESO 383-G087	7.9	7.78	N	...
ESO 445-G089	6.7	9.60	B	...
IC 4710	8.9	8.48	N	NSC ^a
IC 5201	6.1	8.76	B	H II ^b
NGC 45	7.8	9.07	N	X-ray ^c
NGC 247	6.9	8.97	N	NSC ^a
NGC 300	6.9	9.09	W	NSC ^a
NGC 1249	5.9	9.41	B	NSC ^a
NGC 1494	7.0	9.10	N	NSC ^a
NGC 1518	7.7	8.24	N	NSC ^a
NGC 1559	5.9	9.93	B	NSC ^a
NGC 1744	6.5	8.92	B	NSC ^a
NGC 1796	5.0	9.05	B	NSC ^a
NGC 2427	7.6	9.80	W	NSC ^a
NGC 3621	6.8	9.80	N	NSC ^a
NGC 4504	6.1	9.57	N	NSC ^a
NGC 4781	6.8	9.82	W	NSC ^a
NGC 5264	9.3	7.84	N	NSC ^a
NGC 5334	5.0	9.70	B	NSC ^a
NGC 5713	4.1	10.35	B	H II/AGN ^d
NGC 6156	5.0	10.67	B	AGN ^e
NGC 7456	5.9	9.55	N	unknown ^f
NGC 7713	6.9	9.11	N	NSC ^a
NGC 7793	7.0	9.33	N	NSC ^g
PGC 3853	6.9	9.24	B	NSC ^a
PGC 48179	8.9	...	W	unknown ^f

NOTE—Col. (1): Galaxy name. Col. (2): Morphological type index. Col. (3): Stellar mass. Col. (4): Flag for the presence or absence of a bar: B = definitely barred; W = weakly barred; N = no bar or lens. Col. (5): Presence of a nucleus and its physical nature from various references: active galactic nucleus (AGN), nuclear star cluster (NSC), and star-forming nucleus (H II).

^aGeorgiev & Böker 2014.

^bPhillips et al. 1983.

^cPossible X-ray nucleus without optical counterpart on the R -band image; Desroches & Ho 2009; Zhang et al. 2009.

^dStarburst-AGN composite nucleus; Yuan et al. 2010.

^eThe AGN may be saturated in the image; Alonso-Herrero et al. 2012.

^fThe physical nature of the nucleus is unknown.

^gBöker et al. 2002.

ESO 380–G001: The galaxy has a star-forming nucleus (Yuan et al. 2010). The bar parameters have to be fixed; otherwise, its length will be unrealistically long. We model its disk break at the edge of the spiral arms. We mask the dust lanes running through the bar. We ignore some outer features seen in the residual image during the fitting and take them into account when estimating the error budget for the bulge.

ESO 380–G006: We mask the dust lanes on the lens and near the bulge.

ESO 440–G011: The galaxy has a weak and flattened bulge. The bar parameters need to be fixed; otherwise, its length will be unrealistically long. We model the disk break at the edge of the spiral arms.

ESO 442–G026: The galaxy is likely to be an edge-on system with a thin and a thick disk, which we provisionally model as a lens and a disk in our decomposition (see Figure 2.16). Its bar/lens identification is undecided (flagged as “?” in Table 1).

ESO 479–G004: The bar parameters have to be fixed otherwise its length will be unrealistically long. We model the disk break at the edge of the spiral arms.

ESO 494–G026: The galaxy has a high- n bulge and a bar. We model the disk break at the edge of the spiral arms and mask dust lanes near the bulge.

ESO 506–G004: The galaxy is barred, and its bulge shows a weak X-shaped feature. We model the disk break at the edge of the spiral arms.

ESO 507–G025: The galaxy is classified as an elliptical in HyperLeda but as an S0 in RC3. We recognize a blue and dusty region around the galaxy center ($\sim 30''$) and model it as an extra disk component. The dust lanes are masked during the fitting.

ESO 582–G012: We model the disk break at the edge of the spiral arms and mask dust lanes near the bulge.

IC 1953: We model the disk break at the edge of the spiral arms and mask dust lanes across the bar and the bulge.

IC 1954: The bulge morphology is dominated by the nuclear bar. We model the disk break at the edge of the spiral arms and mask dust lanes near the bulge.

IC 1993: We model the disk break at the edge of the spiral arms.

IC 2006: The galaxy is classified as an elliptical in HyperLeda but as an S0 in RC3, and Huang et al. (2013a) discovered some substructures in it. It has a nuclear lens and an inner lens.

IC 2035: In addition to an extremely compact bulge, the galaxy hosts a short bar, two lenses, and an underlying disk that exhibits different orientation. The inner lens is difficult to model unless the outer lens is modeled simultaneously.

IC 2051: The galaxy is barred. We model its disk break at the edge of the spiral arms and mask dust lanes near the bulge.

IC 2056: The galaxy has an NSC (Georgiev & Böker 2014). The bulge exhibits nuclear spiral arms. We model the gentle disk break at the edge of the spiral arms.

ICC 2367: We model the disk break at the bar radius.

IC 2522: The galaxy has a more flattened bulge than the disk.

IC 2537: We model the disk break at the edge of the spiral arms and mask the dust lane near the bulge.

IC 2560: The nucleus appears to be bluer than the surrounding bulge and is classified as Seyfert 2 by Yuan et al. (2010). The galaxy has a boxy/peanut bulge. We model the disk break at the bar radius ($\sim 50''$) but ignore the outer disk break at the edge of the spiral arms ($\sim 75''$), which is treated as an outer feature when estimating bulge errors. We mask the dust lane running through the bar.

IC 2627: The galaxy has a compact bulge.

IC 3253: The bulge has a large Sérsic index ($n \approx 7$). The broken disk is modeled with a Sérsic function.

IC 4214: The bulge is well embedded in the lens or fat bar.

IC 4329: The galaxy is weakly barred. There is no disk break associated with the weak bar. We need to fix some parameters of the bar component to ensure a reasonable fitting.

IC 4444: There is a bright star close to the center. The galaxy has a lens. We model the disk break at the edge of the spiral arms.

IC 4538: We model the disk break at the edge of the spiral arms and mask dust lanes near the bulge.

IC 4618: The nucleus appears to be bluer than the surrounding bulge. The bent bar is modeled with an $m = 2$ bending mode. We model the disk break at the bar radius. We mask the dust lanes near the bulge.

IC 4646: We model the gentle disk break at the edge of the spiral arms.

IC 4845: The galaxy shows a Type III disk profile.

IC 4901: The galaxy has a short bar, but it is not a nuclear bar, as it is significantly longer than the bulge size. The galaxy has a two-disk configuration. We ignore the suspected weak gentle disk break at the end of the spiral arms.

IC 4946: The galaxy is barred and possibly has a boxy/peanut bulge. We mask the dust lanes near the bulge.

IC 4991: A ring-like pattern shows up on the residual image. As we are not able to identify a realistic ring structure and are unsure about its physical nature, we attribute this pattern to artifacts and do not model it.

IC 5240: The galaxy has a boxy/peanut bulge, a strong bar, and a broken disk with weak spiral arms. It is part of the training sample presented in [Gao & Ho \(2017\)](#). Here we show the decomposition results of the model that includes all the above features (Model4 in their Table 9). Note that the uncertainties are different from those presented in their Table 9, since we include the model-induced uncertainties in this study.

IC 5267: The galaxy has an inner disk whose surface brightness profile is reminiscent of a lens. The outer ring is visible on the residual image. The dust lanes across the bulge is masked during the fitting.

IC 5273: The galaxy has a flattened bulge and a bar. Its disk shows a smooth break and is lopsided.

IC 5325: We model the disk break at $\sim 12''$ but ignore the outer disk break at the edge of the spiral arms, which is treated as an outer feature when estimating bulge errors.

IC 5332: The NSC ([Georgiev & Böker 2014](#)) manifest itself as an abrupt change in color profile. The galaxy is angularly so large that simultaneously solving for the sky level during the fitting is impossible. So we fix the sky level to the value obtained via the direct approach. We use two disk components to account for the plateau in the surface brightness profile at $\sim 50''$ and the underlying extended disk.

NGC 150: The galaxy has a starburst–AGN composite nucleus ([Yuan et al. 2010](#)). We model the disk break at the bar radius.

NGC 151: The galaxy has an almost end-on bar. The broken disk is well-described by a Sérsic function.

NGC 210: The galaxy has a nuclear ring. The spiral arms/pseudo outer ring starts at the ends of the lens/bar. The disk break at the edge of the spiral arms is not modeled, as it is regarded as an outer feature. The dust lanes on the lens/bar are not masked because they are far away from the bulge.

NGC 245: The parameters of the weak bar have to be fixed. We model the disk break at the bar radius. The lopsided disk is modeled with an $m = 1$ Fourier mode.

NGC 254: The galaxy has an inner lens and an outer ring. Inside $\sim 5''$, we find fine structures indicative of the presence of a nuclear ring and a nuclear bar. This galaxy was used in [Gao & Ho \(2017\)](#) to illustrate that outer lenses/rings can be ignored for the purposes of bulge decomposition. Here we present the full details of its decomposition, with the outer ring included in the model.

NGC 255: The galaxy has a highly flattened bulge. We model the disk break at the bar radius but ignore the outer disk break at the edge of the spiral arms, treating it as an outer feature when estimating bulge errors.

NGC 289: The galaxy is barred and has a two-disk configuration, with an inner disk resembling a lens due to the tightly wound spiral arms and a diffuse outer disk on which the arms unfold. We ignore the outer disk break at the edge of the spiral arms ($\sim 100''$), treating it as an outer feature when estimating bulge errors. We mask dust lanes near the bulge.

NGC 434: The galaxy has a bar whose α and β are fixed. We model the disk break that manifests as the spiral arms winding back to themselves. We mask the dust lanes near the bulge and along the spiral arms.

NGC 578: The galaxy has a weak bar. We model the disk break at the edge of the spiral arms. The disk is slightly lopsided. We mask central dust lanes during the fitting.

NGC 584: The galaxy is classified as an elliptical in both HyperLeda and RC3, but is recognized as an S0 in [Huang et al. \(2013a\)](#). It has a nuclear lens and an inner lens.

NGC 613: The bar parameters are fixed to prevent it from being unrealistically long. We model the inner disk break at the bar radius but ignore the outer disk break ($\sim 150''$), which is treated as an outer feature when estimating bulge errors.

NGC 615: The galaxy has a lens. We model the disk break at the edge of the spiral arms and mask the dust lanes near the bulge.

NGC 685: We ignore the suspected weak nucleus. The galaxy has a flattened bulge and a bar. Its broken disk is modeled with a Sérsic function. We mask the dust lanes on the bar.

NGC 701: The galaxy has a highly flattened bulge. Its broken disk is modeled with a Sérsic function. We mask the dust lanes around the bulge.

NGC 782: The galaxy is barred whose α and β are fixed. We model the disk break at the inner ring.

NGC 895: We model the disk break at the edge of the spiral arms and mask the spiral dust lanes approaching the bulge.

NGC 908: We model the disk break at the edge of the spiral arms and mask dust lanes near the bulge.

NGC 936: The galaxy has a bar that is enclosed by an inner ring. Its structural layout is similar to that of NGC 1533.

NGC 945: The galaxy has a weak bulge, a thin bar, and a broken disk with prominent spiral arms. It is part of the training sample presented in [Gao & Ho \(2017\)](#). Here we show the decomposition results of the model that includes all the above features (Model3 in their Table 11). Note that the uncertainties are different from those presented in their Table 11, since we include the model-induced uncertainties in this study.

NGC 986: We model the disk break at the bar radius as an inner lens/ring, but ignore the outer disk break at the edge of the spiral arms and treat it as an outer feature when estimating bulge errors. We mask the dust lanes running through the bar and the bulge.

NGC 1022: The star-forming nucleus ([Yuan et al. 2010](#)) is distinctly blue. The galaxy has a bar that is enclosed by an inner ring/lens. We mask the circumnuclear dust lanes during the fitting.

NGC 1042: The nucleus is an NSC and an AGN ([Shields et al. 2008](#); [Georgiev & Böker 2014](#)). We model the disk break at the edge of the spiral arms. An extra disk component is needed to account for the bar-like pattern produced by the spiral arms winding onto the bulge; otherwise, the bulge will be unrealistically flattened.

NGC 1068: The galaxy has a Seyfert 2 nucleus ([Seyfert 1943](#)), a flattened bulge that hosts a nuclear bar, and a prominent lens. The nucleus is recently classified as a starburst–AGN composite nucleus by [D’Agostino et al. \(2018\)](#). We mask the dust lanes near the center. The galaxy is angularly so large that simultaneously solving the sky level during the fitting is impossible. So we fix the sky level to the value obtained via the direct approach.

NGC 1079: The galaxy has an inner ring/lens. We ignore the disk break at the edge of the spiral arms, which is treated as an outer feature when estimating bulge errors.

NGC 1084: The inner broken disk is modeled with a Sérsic function.

NGC 1087: The galaxy has a flattened bulge. We ignore the disk break at the edge of the spiral arms, because the overall disk is well-described by an exponential function. We mask the circumnuclear dust lanes during the fitting.

NGC 1090: The galaxy is barred. We model its disk break at the edge of the spiral arms and mask the circumnuclear dust lanes.

NGC 1097: The galaxy has a LINER/Seyfert 1 nucleus ([Maiolino et al. 1997](#); [Ho 2009](#)) and a prominent nuclear star-forming ring well embedded in a strong bar whose α and β are fixed during the fitting. We ignore the disk break at the edge of the spiral arms and treat it as an outer feature when estimating bulge errors. The dust lanes along the bar are masked. The galaxy is angularly so large that simultaneously solving the sky level during the fitting is impossible. So we fix the sky level to the value obtained via the direct approach.

NGC 1179: The galaxy has a short bar whose α and β are fixed during the fitting. We model the disk break at the bar radius but ignore the outer disk break at the edge of the spiral arms, which is treated as an outer feature when estimating bulge errors.

NGC 1187: We fix α and β of the Ferrer bar during the fitting. We model the disk break at the bar radius but ignore the outer disk break at the edge of the spiral arms, treating it as an outer feature when estimating bulge errors. We mask the dust lanes running across the bar.

NGC 1201: The galaxy contains an inner lens and an outer lens. But unlike normal cases with two lenses of different sizes, in this case the inner lens fills the outer lens in one dimension. Therefore, we also model the outer lens to avoid potential bias of the bulge parameters. A possible outer ring is visible on the residual image. There is a nuclear bar with a size of $\sim 5''$ and a PA $\approx 10^\circ$.

NGC 1232: The galaxy has a nuclear bar. We model the disk break at the edge of the spiral arms. The galaxy is angularly so large that simultaneously solving the sky level during the fitting is impossible. So we fix the sky level to the value obtained via the direct approach.

NGC 1255: The galaxy has a flattened bulge. The disk is lopsided and breaks at the edge of the spiral arms.

NGC 1291: The galaxy has a nuclear bar and a large-scale bar embedded in a lens/ring. The dust lanes near the bulge are masked. The galaxy is angularly so large that simultaneously solving the sky level during the fitting is impossible. So we fix the sky level to the value obtained via the direct approach.

NGC 1292: We model the disk break at the edge of the spiral arms.

NGC 1300: The galaxy has a prominent nuclear ring. We model the disk break at the bar radius but ignore the outer disk break at the edge of the spiral arms, treating it as an outer feature when estimating bulge error. The dust lanes running through the bar are masked during the fitting.

NGC 1302: This is a barred galaxy with an inner ring and an outer ring. This galaxy was used in Gao & Ho (2017) to illustrate that the outer lenses/rings can be ignored for the purposes of bulge decomposition. Here we present the full details of its decomposition, with the outer ring included in the model.

NGC 1309: The galaxy has a Type III disk profile.

NGC 1317: The galaxy has a lens/weak bar. We find residual spiral patterns outside the outer ring.

NGC 1326: The galaxy has a bar, a nuclear ring, an inner ring, and an outer ring. It is part of the training sample presented in Gao & Ho (2017). Here we show the decomposition results that include the inner and outer ring, with the nuclear ring unmasked (Model3 in their Table 8). Note that the uncertainties are different from those presented in their Table 8, since we include the model-induced uncertainties in this study.

NGC 1350: We model the disk break at the inner ring and ignore that at the outer ring.

NGC 1353: We mask the dust lanes near the bulge during the fitting.

NGC 1357: The galaxy has a two-disk configuration, with the inner blue disk showing prominent spiral arms and the outer red disk showing weak spiral arms. It is part of the training sample presented in Gao & Ho (2017). Here we show the decomposition results that include all the above features (Model3 in their Table 4). Note that the uncertainties are different from those presented in their Table 4, since we include the model-induced uncertainties in this study.

NGC 1365: The galaxy has a Seyfert 1.8 nucleus (Véron-Cetty & Véron 2010), but it is recently classified as a starburst–AGN composite nucleus by D’Agostino et al. (2018). We model the disk break at the edge of the spiral arms. The dust lanes running through the bar are masked.

NGC 1367: The galaxy has a short bar whose α and β are fixed during the fitting. It has a two-disk configuration: a red inner disk and a blue outer disk.

NGC 1380: The galaxy is likely to be an edge-on system with a thin and a thick disk, which we provisionally model as a lens and a disk in our decomposition (see Figure 2.94). Its bar/lens identification is undecided (flagged as “?” in Table 1). The “lens” component is not perfectly modeled by the Sérsic function. The dust lane running through the bulge is masked.

NGC 1385: We ignore the gentle disk break at $\sim 60''$ and treat it as an outer feature when estimating bulge errors. We mask the dust lanes to the north of the bulge.

NGC 1386: The bulge is distinctly blue compared to the disk. The disk has a Type II profile. We tried to mask the majority of the dust lanes.

NGC 1387: The nuclear ring is readily recognizable in the residual pattern and the color map. The galaxy is barred and its disk is broken at the bar radius.

NGC 1398: We model the disk break at the bar radius but ignore the outer disk break at $\sim 150''$, which is treated as an outer feature when estimating bulge errors. The galaxy is angularly so large that simultaneously solving the sky level during the fitting is impossible. So we fix the sky level to the value obtained via the direct approach.

NGC 1400: The galaxy is classified as an elliptical in HyperLeda but as an S0 in RC3. We recognize a lens at $\sim 20''$. The dust lanes are masked during the fitting.

NGC 1411: The galaxy has a nuclear lens and an inner lens. It is part of the training sample presented in Gao & Ho (2017). Here we show the decomposition results of the model that includes the two lenses (Model3 in their Table 2). Note that the uncertainties are different from those presented in their Table 2, since we include the model-induced uncertainties in this study.

NGC 1415: The galaxy has a lens. We mask the dust lanes near the bulge during the fitting.

NGC 1417: The galaxy has a high- n bulge. We model the disk break at the edge of spiral arms.

NGC 1425: The galaxy has a high- n bulge and a lens.

NGC 1433: The galaxy has a nuclear ring and a strong bar. We model the disk break at the bar radius and mask the dust lanes running through the bar.

NGC 1436: We model the disk break at $\sim 40''$. An extra disk component is needed to account for the bar-like pattern produced by the spiral arms winding onto the bulge; otherwise, the bulge orientation and ellipticity will be incorrect.

NGC 1452: We model the disk break at the bar radius but ignore the outer disk break at the edge of the spiral arms, which is treated as an outer feature when estimating bulge errors. The disk shows weak spiral arms.

NGC 1493: The galaxy has an NSC (Georgiev & Böker 2014). Recently it is designated as an AGN candidate in X-rays, though it was classified as an H II nucleus in the optical (She et al. 2017a,b). We fix α and β of the bar component during the fitting. We model the disk break at the bar radius but ignore the outer disk break at the edge of the spiral arms, treating it as an outer feature when estimating bulge errors. We mask the dust lanes near the bulge.

NGC 1512: The galaxy and NGC 1510 form a starburst pair (Meurer et al. 2006). It has a starburst nucleus (Grier et al. 2011) and a nuclear ring. We model the disk break at the bar radius but ignore the outer disk break at the edge of the spiral arms, treating it as an outer feature when estimating bulge errors. We mask the circumnuclear dust lanes and the dust lanes on the leading edge of the bar.

NGC 1527: The galaxy has an inner lens and a weak outer lens.

NGC 1533: The galaxy is barred and its disk is broken roughly at the bar radius. A ring-like pattern in the central $10''$ implies the presence of a barlens—a face-on version of a boxy/peanut bulge. This galaxy is part of the training sample presented in Gao & Ho (2017). Here we show the decomposition results of Model2 in their Table 7. Note that the uncertainties are different from those presented in their Table 7, since we include the model-induced uncertainties in this study.

NGC 1537: The galaxy is classified as an elliptical in HyperLeda but as a weakly barred S0 in RC3. We recognize it as an S0 that has a nuclear lens and an inner lens.

NGC 1543: The galaxy has a nuclear bar, a large-scale bar, an inner lens/ring, and an outer ring.

NGC 1553: The galaxy has a nuclear lens and an inner lens/ring. Thus, its model construction is similar to that of NGC 1411.

NGC 1566: The galaxy has an NSC (Georgiev & Böker 2014). It is classified as a Seyfert 1 nucleus in the optical (Sosa-Brito et al. 2001; da Silva et al. 2017). An extra disk component is needed to account for the lens-like pattern produced by the spiral arms winding onto the bulge. We ignore the disk break at the edge of the spiral arms and treat it as an outer feature when estimating bulge errors. We mask circumnuclear dust lanes during the fitting.

NGC 1574: There is a bright foreground star on the galaxy disk. The bar is embedded in a lens. An outer ring is only visible on the residual image.

NGC 1617: We model the disk break at $\sim 100''$. The weak spiral pattern in the disk is visible on the residuals.

NGC 1637: The nucleus manifests itself as an abrupt change in the optical color profile. The galaxy has a dominant point source in X-rays (Zhang et al. 2009; Cisternas et al. 2013), which suggests the presence of an AGN. We fix α and β of the bar component during the fitting. The disk is significantly lopsided. We model the disk break at the edge of the spiral arms. We mask the dust lanes near the bulge.

NGC 1640: The nucleus manifests itself as a abrupt change in the optical color profile. The galaxy has a dominant point source in X-rays (Zhang et al. 2009; Cisternas et al. 2013), which suggests the presence of an AGN. We fix α and β of the bar component during the fitting. We model the disk break at the bar radius but ignore the outer disk break at the edge of the spiral arms, treating it as an outer feature when estimating bulge errors.

NGC 1667: The galaxy has a low-luminosity Seyfert 2 nucleus (Barth et al. 1999; Véron-Cetty & Véron 2010), a nuclear bar, and a two-disk configuration (inner blue disk and outer red disk).

NGC 1672: The galaxy has a dusty but overall blue bulge and a bar embedded in a lens. We model the disk break at the edge of the spiral arms.

NGC 1688: The galaxy is reported to host an NSC by Carollo et al. (2002) and Seth et al. (2008), but Georgiev & Böker (2014) find no measurable NSC. There is no X-ray detection in the nucleus (Foord et al. 2017). The galaxy has a highly flattened bulge. We fix α and β of the bar component during the fitting. The disk is significantly lopsided. We model the disk break at the edge of the spiral arms. We mask the dust lanes near and on the bulge.

NGC 1703: We model the disk break at the edge of the spiral arms.

NGC 1723: We model the disk break at the bar radius but ignore the outer disk break at the edge of the spiral arms, treating it as an outer feature when estimating bulge errors. We fix α and β of the bar component during the fitting.

NGC 1726: There are dust lanes near the galaxy center, and we mask them during the fitting.

NGC 1784: We ignore both the gentle inner and outer disk breaks. The dust lanes across the bar and the bulge are masked.

NGC 1792: We model the disk break at $\sim 60''$.

NGC 1808: The galaxy has a Seyfert 2 nucleus according to (Brightman & Nandra 2011a), while (Yuan et al. 2010) classified it as an H II nucleus. The dusty and star-forming bulge is embedded in a lens/bar. We mask the dust lanes near the bulge.

NGC 1832: We ignore the gentle inner and outer disk breaks. We mask the dust lanes near the bulge.

NGC 1947: There are many foreground stars throughout the image. We mask the dust lanes across the bulge.

NGC 1954: The lens has a different orientation from that of the diffuse outer disk.

NGC 1964: There is a bright star near the bulge. The galaxy has a dusty oval. We mask the dust lanes near the bulge.

NGC 2082: There are many foreground stars throughout the image. The galaxy has a weak NSC (Carollo et al. 2002; Seth et al. 2008) that does not affect the bulge much. The galaxy has a bulge more flattened than the disk. We model the disk break at the edge of the spiral arms.

NGC 2090: The galaxy has a two-disk layout: inner red disk/lens (perhaps due to dust) and outer blue disk.

NGC 2139: The galaxy has an NSC (Georgiev & Böker 2014) and a highly flattened, blue bulge. The lopsided disk shows a Type II profile.

NGC 2196: The galaxy has an NSC (Carollo et al. 2002) that is inactive (Hunt & Malkan 2004). We ignore the gentle disk break at $\sim 50''$ because the overall disk is well-described by an exponential function.

NGC 2207: The galaxy is merging with IC 2163, but its overall morphology is regular. The galaxy has a nuclear ring and a nuclear bar. We model the disk break at the edge of the spiral arms. An extra disk component is needed to account for the ring/plateau feature at $\sim 30''$.

NGC 2217: The galaxy has a bar, and an inner and outer ring. The model includes all these features, because it is difficult to achieve reasonable fits for the bar and inner ring without the outer ring in the model. A nuclear ring with a size of $\sim 10''$ is visible in the residual pattern.

NGC 2223: The broken disk is modeled with a Sérsic function. We fix α and β of the bar component during the fitting.

NGC 2397: The galaxy has an NSC (Carollo et al. 1997; Seth et al. 2008). We ignore the disk break at $\sim 30''$, because the overall disk is well-described by an exponential function. We mask the dust lanes near the bulge.

NGC 2417: The suspected gentle disk break at $\sim 40''$ is ignored.

NGC 2442: We model the disk break at the edge of the spiral arms. We mask the dust lanes around the bulge.

NGC 2525: The galaxy has a photometrically distinct nucleus that is bluer than its surroundings. We mask the dust lanes around the bulge and along the bar.

NGC 2559: The galaxy has a dusty and irregular bulge. We model the disk break at the bar radius but ignore the outer disk break at the edge of the spiral arms, treating it as an outer feature when estimating bulge errors. We mask the major dust lanes along the bar and spiral arms.

NGC 2566: The galaxy has a blue star-forming bulge. We model the disk break at the bar radius but ignore the outer disk break at the edge of the spiral arms, treating it as an outer feature when estimating bulge errors. We mask the dust lanes along the bar.

NGC 2640: The galaxy is weakly barred, and its disk is broken at the bar radius. A large number of foreground stars are projected on top of the galaxy.

NGC 2695: The galaxy has an inner lens.

NGC 2698: The galaxy is likely to be an edge-on system with a thin and a thick disk, which we provisionally model as a lens and a disk in our decomposition (see Figure 2.147). Its bar/lens identification is undecided (flagged as “?” in Table 1).

NGC 2708: The galaxy has an exponential lens/bar. We mask the dust lanes on the lens and near the bulge.

NGC 2763: The galaxy has a very short bar whose size is comparable to that of the bulge. Thus, we regard it as a nuclear bar.

NGC 2781: The galaxy has a nuclear ring, an inner lens/ring, and an outer ring. We do not find any signature of a bar.

NGC 2784: The galaxy has an inner lens and outer lens. It is part of the training sample presented in Gao & Ho (2017). Here we show the decomposition results of Model3 in their Table 3. Note that the uncertainties are different from those presented in their Table 3, since we include the model-induced uncertainties in this study.

NGC 2811: The inner empty region ($\lesssim 30''$) on the image and the peak in the ellipticity profile suggest that there may be a bar, although modeling a bar is difficult and uncertain due to the fact that the galaxy is highly inclined and the bar is seen close to end-on. A composite disk model is constructed to make sure that the disk break at the inner ring is properly taken into account.

NGC 2835: The galaxy has an NSC (Georgiev & Böker 2014) and a short bar. We model the disk break at the bar radius but ignore the outer disk break at the edge of the spiral arms, treating it as an outer feature when estimating bulge errors. We mask the dust lanes near the bulge.

NGC 2848: We ignore the suspected weak disk break at the edge of the spiral arms.

NGC 2889: The galaxy has a short and weak bar whose α and β are fixed. We mask the circumnuclear dust lanes. The broken disk is modeled with a Sérsic function. An extra disk component is included to account for the diffuse outskirts.

NGC 2907: This is an almost edge-on galaxy with a thick disk that leads to an underestimate of its inclination angle by Ho et al. (2011). We mask the dust lanes running through the thin disk.

NGC 2935: The galaxy has a nuclear ring. Its bar is embedded in a lens/ring structure. We model the disk break at the edge of the spiral arms.

NGC 2947: The galaxy has a distinctly blue nucleus. We model its disk break at $\sim 15''$.

NGC 2983: The galaxy is barred, and its disk is broken at the bar radius. Its model construction is similar to that of NGC 1533.

NGC 3001: The galaxy has a distinctly blue nucleus of unknown nature (Véron-Cetty & Véron 1986). An extra disk component must be included to account for the tightly wound spiral arms that resemble a bar near the bulge; otherwise, the bulge orientation and ellipticity will be incorrect. In addition, the bulge orientation is constrained to be aligned with the disk. The size of the original PSF image is not large enough, and we build an adequate one using the IRAF task `psf`.

NGC 3038: An extra disk component is needed to account for the extra light around the bulge; otherwise, the bulge will be unrealistically large. The dust lane around the bulge is masked.

NGC 3052: The broken disk is modeled with a Sérsic function.

NGC 3054: Significant sky gradient is present in the residual image. We model the gentle disk break at the bar radius. We fix α and β of the bar component; otherwise, their values become unrealistic.

NGC 3056: The galaxy has an inner lens/ring. The residual pattern seems to suggest the presence of a nuclear lens, but we do not find significant signatures of substructures inside $\sim 20''$ from inspection of its image and isophotal analysis. So we do not pursue further refinements of the model.

NGC 3059: The galaxy has a highly flattened bulge. We mask the dust lanes along the bar. The broken disk is modeled with a Sérsic function. In addition, we include an extra disk component to account for the diffuse outskirts.

NGC 3095: We mask the dust lanes along the bar. We model the disk break at the bar radius but ignore the outer disk break at the edge of the spiral arms, treating it as an outer feature when estimating bulge errors.

NGC 3100: The galaxy has two lenses, but their configuration is unlike that of a typical inner-outer lens configuration. One lens fills the other in one dimension; therefore, we model the two lenses together. There are dust lanes near the bulge, which we mask during the fitting.

NGC 3108: This is an interesting case: a huge classical bulge is assembling a diffuse disk around itself (Hau et al. 2008).

NGC 3124: The galaxy has a short and curved bar whose α and β are fixed. The broken disk is modeled with a Sérsic function.

NGC 3145: We model the broken disk with a Sérsic function.

NGC 3223: We model the disk break at $\sim 90''$.

NGC 3261: We fix α and β of the bar component during the fitting. We model the disk break at the bar radius but ignore the outer disk break at the edge of the spiral arms ($\sim 60''$), treating it as an outer feature when estimating bulge errors.

NGC 3271: Fortunately, we do not need to deal with the disk break associated with the bar, as the bulge is well-embedded in the thick bar. The circular dust lane at the galaxy center is masked during the fitting. We find fine structures that suggest the presence of a nuclear bar roughly aligned with the large-scale bar.

NGC 3275: The bar parameters are fixed, or else the bar will be unrealistically long. We model the disk break at the bar radius but ignore the outer disk break at $\sim 50''$, treating it as an outer feature when estimating bulge errors. We mask the dust lane across the bar.

NGC 3281: The galaxy is classified as Seyfert 2 in the optical (Véron-Cetty & Véron 2010), but we find no sign of a nucleus, which is probably obscured by the dust. The galaxy is well-described by a Sérsic bulge and an exponential disk. We mask the dust lanes running through the center.

NGC 3313: The galaxy has a prominent nuclear star-forming ring. We model the disk break at the bar radius. We carefully mask the bright star near the bulge.

NGC 3318: The galaxy has a compact bulge. We fix α and β of the weak bar during the fitting. We model the disk break at the bar radius.

NGC 3358: The galaxy has an inner lens. The outer disk break/ring is also modeled, or else the bulge will be underestimated.

NGC 3366: The galaxy hosts an inactive nucleus (Siebenmorgen et al. 2008). The broken disk is modeled with a Sérsic function. We include an extra disk component to account for the diffuse outskirts.

NGC 3450: We fix α and β of the bar component during the fitting. We model the disk breaks at the bar radius and at the edge of the spiral arms.

NGC 3513: There is noticeable residual light at the center of the galaxy. Since Georgiev & Böker (2014) did not find a measurable NSC, we do not include a PSF component to account for the residuals. The galaxy has a highly flattened bulge. We fix α and β of the bar component during the fitting. We model the disk break at the bar radius but ignore the outer disk break at the edge of the spiral arms ($\sim 60''$), treating it as an outer feature when estimating bulge errors. We mask the dust lanes near the bulge.

NGC 3521: The galaxy has an emission-line nucleus classified as H II or LINER (Ho et al. 1997). Georgiev & Böker (2014) did not find any measurable NSC. We use two exponential components with different ellipticities to model the disk.

NGC 3568: We use two components with slightly different orientations and ellipticities to model the disk. We mask the dust lanes near the bulge.

NGC 3660: We model the disk break at the bar radius but ignore the outer disk break at the edge of the spiral arms, treating it as an outer feature when estimating bulge errors. We mask the dust lanes running through the bar and the bulge.

NGC 3672: We model the disk break at the edge of the spiral arms.

NGC 3673: The galaxy has a distinctly blue nucleus and a weakly boxy bulge. We model the disk break at the bar radius but ignore the outer disk break at the edge of the spiral arms, treating it as an outer feature when estimating bulge errors. We mask the dust lanes near the bulge.

NGC 3763: The broken disk is modeled with a Sérsic function. Some of the bar parameters are fixed. We mask the dust lanes around the bulge.

NGC 3783: The galaxy has a Seyfert 1/1.5 nucleus (Véron-Cetty & Véron 2010; Yuan et al. 2010). We model the disk break at the bar radius and the anti-truncation at $\sim 60''$.

NGC 3882: There are many foreground stars throughout the image. We model the disk break at the bar radius. We mask the dust lanes near the bulge.

NGC 3885: The galaxy has a lens. We mask all the major dust lanes during the fitting.

NGC 3887: The galaxy has a distinctly blue nucleus. We model the disk break at the bar radius. We model the spiral dust lanes approaching the galaxy center.

NGC 3892: This barred galaxy has an inner ring and an outer ring. In addition, we need to include a compact nucleus, which is modeled with a PSF component, or else the Sérsic index of the bulge would be unrealistically large.

NGC 3904: The galaxy is classified as an elliptical in both HyperLeda and RC3, but is recognized as a possible S0 in Huang et al. (2013a). It has two lenses, one filling the other in one dimension. We model both lenses simultaneously.

NGC 3955: The galaxy hosts a weak nucleus of unknown nature (Yuan et al. 2010) that appears to be abruptly bluer than its surrounding. We mask dust-obscured regions within $\sim 40''$. The galaxy has a two-disk configuration: an inner dusty but blue disk and an outer smooth one.

NGC 3981: We fix α and β of the bar component during the fitting. The galaxy has a two-disk configuration: an inner disk with sharply truncated spiral arms and an outer diffuse one. We mask the dust lanes near the bulge. Note that there are significant residuals of unknown origin at the galaxy center.

NGC 4024: The galaxy is barred, and its disk break at the bar radius is weak. Its model construction is similar to that of NGC 1533.

NGC 4027: The galaxy has a flattened bulge. We model the inner disk break but ignore the outer one, which is treated as an outer feature when estimating bulge errors. The disk is significantly lopsided. We mask the dust lanes around the bulge.

NGC 4030: Georgiev & Böker (2014) found an NSC at the galaxy center, but we find no sign of an unresolved point source on the CGS image. We need to include an extra disk component in the model; otherwise, the bulge will be unrealistically large.

NGC 4033: The galaxy is classified as an elliptical in both HyperLeda and RC3, but is recognized as a possible S0 in Huang et al. (2013a). It has a nuclear lens.

NGC 4050: We model the disk break at the bar radius but ignore the outer disk break at $100''$, treating it as an outer feature when estimating bulge errors. We mask the dust lanes around the bulge.

NGC 4094: We model the disk break at the edge of the spiral arms. We mask the dust lanes around the bulge.

NGC 4304: We model the disk break at the bar radius but ignore the outer disk break at the edge of the spiral arms, treating it as an outer feature when estimating bulge errors. We mask the dust lanes running through the bar and the bulge.

NGC 4373A: The galaxy is likely to be an edge-on system with a thin and a thick disk, which we provisionally model as a lens and a disk in our decomposition (see Figure 2.203). Its bar/lens identification is undecided (flagged as “?” in Table 1). The dust lane running through the bulge is masked during the fitting.

NGC 4462: We model the disk break at the bar radius but ignore the outer disk break at the edge of the spiral arms, treating it as an outer feature when estimating bulge errors. We mask the dust lanes running through the bar and around the bulge.

NGC 4487: The galaxy has an NSC (Georgiev & Böker 2014) and a flattened bulge. We model the disk break at the edge of the spiral arms. We mask the dust lanes near the bulge.

NGC 4546: The galaxy is likely to be an edge-on system with a thin and a thick disk, which we provisionally model as a lens and a disk in our decomposition (see Figure 2.206). Its bar/lens identification is undecided (flagged as “?” in Table 1).

NGC 4593: The galaxy has a Seyfert 1 nucleus (Véron-Cetty & Véron 2010; Yuan et al. 2010), a bar embedded in a lens/ring component, and a disk break at the edge of the spiral arms. The dust lanes around the bulge are masked.

NGC 4594: The Sombrero galaxy is an edge-on galaxy with a thick disk that led to an underestimate of its inclination angle by Ho et al. (2011). We mask the major dust lane running through the thin disk.

NGC 4603: We model the broken disk with a Sérsic function.

NGC 4632: The galaxy hosts an H II nucleus (Decarli et al. 2007; Gavazzi et al. 2013). We model the disk break at $\sim 60''$. We mask the dust lanes near the bulge.

NGC 4650: We model the gentle disk break at the bar radius and mask the dust lanes near the bulge.

NGC 4653: We ignore the gentle disk break at $\sim 90''$.

NGC 4684: We attribute the lens-like structure with a size of $\sim 20''$ as the bulge. Otherwise, the galaxy would have $B/T = 0$. The compact nucleus is modeled as a PSF component. The central dust lane is masked during the fitting.

NGC 4691: The nucleus is classified as an H II nucleus in the optical (Yuan et al. 2010), but there is no evidence for an obscured AGN in the X-rays (Maiolino et al. 2003). However, Véron-Cetty & Véron (2010) classified it as Seyfert 1 nucleus. The galaxy has a highly flattened bulge. We model the disk break at the bar radius. We mask the dust lanes along the bar and on the bulge.

NGC 4697: The galaxy is classified as an elliptical in both HyperLeda and RC3, but is recognized as an S0 in Huang et al. (2013a). The galaxy is likely to be an edge-on system with a thin and a thick disk, which we provisionally model as a lens and a disk in our decomposition (see Figure 2.215). Its bar/lens identification is undecided (flagged as “?” in Table 1).

NGC 4699: The galaxy has a nuclear bar and two lenses.

NGC 4727: The galaxy has a short bar whose α and β are fixed during the fitting. It has a two-disk configuration: an inner disk with spiral arms and an outer diffuse disk without discernible spiral patterns.

NGC 4731: The galaxy has a highly flattened bulge. We model the disk break at the bar radius but ignore the outer disk break at the edge of the spiral arms, treating it as an outer feature when estimating bulge errors. We mask the dust lanes near the bulge.

NGC 4802: The galaxy has a dusty but overall blue bulge, which is indicative of ongoing star formation. In addition, we recognize a nuclear lens and an inner lens. We mask the dust lanes around the bulge. The compact nucleus is modeled using a PSF component.

NGC 4825: The galaxy is classified as an elliptical in HyperLeda but as an S0 in RC3. The central dust lane running through the bulge is masked during the fitting.

NGC 4856: The galaxy is relatively edge-on, but its bar is still readily recognizable. Its disk is broken at the bar radius.

NGC 4899: We model the disk break at the edge of the spiral arms and mask the dust lanes on the bulge.

NGC 4902: We model the disk break at the bar radius but ignore the outer disk break at the edge of the spiral arms, treating it as an outer feature when estimating bulge errors. We mask the dust lanes near the bulge during the fitting.

NGC 4930: We fix α and β of the bar component; otherwise, it will be unrealistically long. We model the disk break at the bar radius.

NGC 4939: The galaxy has tightly wound spiral arms. We ignore the possible gentle disk break beyond $\sim 170''$.

NGC 4941: The galaxy has a Seyfert 2 nucleus (Rush et al. 1993; Véron-Cetty & Véron 2010), but whether we include a nucleus in the model or not does not affect the bulge parameters much. The galaxy probably hosts a nuclear bar. The bulge is embedded in a lens.

NGC 4947: The galaxy has an H II nucleus (Véron-Cetty & Véron 1986). The bulge orientation is constrained to be the same as that of the disk, or else the bulge will turn to fit the spiral arms winding onto itself. We model the broken disk with a Sérsic function. We find some positive residuals beyond $\sim 60''$ but do not include an extra component to account for them. We treat them as outer features when estimating bulge errors. We mask the dust lanes near the bulge during the fitting.

NGC 4965: The galaxy has a distinctly blue nucleus of unknown nature. We model the disk break at the edge of the spiral arms. Note that there is a bright blob to the north-east of the galaxy, which causes noticeable residuals in the background.

NGC 4981: We fix α and β of the weak bar during the fitting. We model the disk break at the bar radius but ignore the outer disk break at the edge of the spiral arms, treating it as an outer feature when estimating bulge errors. We mask the dust lanes on the bulge and the bar.

NGC 4984: The galaxy has an inner lens and outer ring. The bulge is distinctly blue compared with the lens and the disk. This galaxy was used in Gao & Ho (2017) to illustrate that outer lenses/rings can be ignored for the purposes of bulge decomposition. Here we present the full details of its decomposition, with the outer ring included in the model.

NGC 4995: The galaxy has a distinctly blue nucleus that is classified as a composite AGN/H II nucleus by Giuricin et al. (1994) but as an H II nucleus by Rush et al. (1993). We model the disk break at $\sim 30''$.

NGC 5026: The galaxy has a bar that is enclosed by an inner ring. An outer ring is visible on the residual image.

NGC 5042: The galaxy has a distinctly blue nucleus of unknown nature. We ignore the gentle disk break at $\sim 140''$. We mask the circumnuclear dust lanes during the fitting.

NGC 5054: The galaxy has an NSC (Georgiev & Böker 2014) and a nuclear ring. We mask the dust lanes near the bulge.

NGC 5068: The galaxy has an NSC (Georgiev & Böker 2014) and a highly flattened bulge. We model the disk break at the bar radius and mask the dust lanes near the bar during the fitting.

NGC 5078: This is an edge-on galaxy with a thick disk that leads to an underestimate of its inclination angle by Ho et al. (2011). We mask the prominent dust lane running through the thin disk.

NGC 5101: We model the disk break at the bar radius. We fix α and β of the bar component, or else the bar will be unrealistically long.

NGC 5121: The galaxy has a lens. We model the disk break at the edge of the spiral arms.

NGC 5134: The galaxy has a distinctly red and inactive nucleus (Koulouridis 2014). The galaxy has a lens. We mask the dust lanes near the bulge.

NGC 5135: The bar is embedded in a lens. We ignore the disk break at the edge of the spiral arms and treat it as an outer feature when estimating bulge errors.

NGC 5156: We model the disk break at the bar radius but ignore the outer disk break at $\sim 60''$, treating it as an outer feature when estimating bulge errors. We mask the dust lanes on the bulge and the bar.

NGC 5188: The center is heavily dust-obscured. The galaxy has a lens. We ignore the disk break at $\sim 60''$ and treat it as an outer feature when estimating bulge errors.

NGC 5247: The galaxy has a dusty but overall blue bulge. We model the disk break at the edge of the spiral arms. Meanwhile, we fix the scale length of the inner part of the disk; otherwise, it will be unrealistically long. We mask the dust lanes on and near the bulge.

NGC 5253: The galaxy has an NSC (Smith et al. 2016) and a starburst bulge. We mask the dust lanes on the bulge. The peculiar pattern in the sky background introduces large sky measurement error.

NGC 5254: We model the broken disk with a Sérsic function.

NGC 5266: We mask the central circular dust lanes along the minor axis of the galaxy.

NGC 5292: The galaxy is well-described by a Sérsic bulge and an exponential disk.

NGC 5324: The galaxy has a nuclear ring. We model the broken disk with a Sérsic function.

NGC 5333: The galaxy has a nuclear lens and an inner lens.

NGC 5339: The galaxy has a distinctly blue nucleus of unknown nature. We model the disk break at the bar radius. We mask the dust lanes along the bar and around the nucleus.

NGC 5468: The galaxy has a compact bulge. An extra disk component is needed to account for the lens-like pattern produced by the spiral arms winding onto the bulge. The broken disk is modeled with a Sérsic function.

NGC 5483: The galaxy has a nucleus of unknown nature. We ignore the positive residuals in the outskirts and treat them as outer features when estimating bulge errors.

NGC 5530: The galaxy has an NSC (Georgiev & Böker 2014). There is a bright saturated star near the center. We model the broken disk with a Sérsic function.

NGC 5556: The galaxy has an NSC (Georgiev & Böker 2014) and a flattened bulge. We model the disk break at the edge of the spiral arms. We mask several dust-attenuated regions around the bulge.

NGC 5597: The galaxy has an H II nucleus (Hunt & Malkan 2004) and a flattened bulge. We model the disk break at the edge of the spiral arms. We mask several dust-attenuated regions around the bulge and on the bar.

NGC 5643: The galaxy has a Seyfert nucleus (Phillips et al. 1983). We model the disk break at the bar radius but ignore the outer disk break at $\sim 60''$, treating it as an outer feature when estimating bulge errors. We mask the dust lanes along the bar and around the bulge.

NGC 5688: The galaxy has an almost end-on bar, whose α and β are fixed. We model the broken disk with a Sérsic function.

NGC 5728: The galaxy has a nuclear ring. We model the disk break at the bar radius but ignore the outer disk break at the edge of the spiral arms, treating it as an outer feature when estimating bulge errors.

NGC 5786: The galaxy has a blue bulge with a large Sérsic index and a short bar. We model the disk break at the edge of the spiral arms. We mask the dust lanes near the bulge. The image shows significant sky gradient introduced by a saturated star.

NGC 5833: The galaxy has a distinctly blue nucleus that is inactive (Greenhill et al. 2002). We ignore the gentle disk break at $\sim 60''$ and treat it as an outer feature when estimating bulge errors. We mask the dust lanes near the bulge.

NGC 5861: The galaxy has a dusty bulge. We model the broken disk with a Sérsic function. We mask the dust lanes on the bulge.

NGC 5885: The galaxy has a blue compact bulge and a short bar whose α and β are fixed. We ignore the gentle disk break at $\sim 100''$ and treat it as an outer feature when estimating bulge errors. We mask the dust lanes near the bulge and along the bar.

NGC 5938: There are many foreground stars throughout the image. We model the disk break at the bar radius but ignore the outer disk break at the edge of the spiral arms, treating it as an outer feature when estimating bulge errors. We mask the dust lanes around the bulge.

NGC 5967: The galaxy has an H II nucleus (Véron-Cetty & Véron 1986) and a weak bar whose parameters have to be fixed. We model the broken disk with a Sérsic function.

NGC 6118: The galaxy has a flattened bulge and a broken spiral disk well-described by a Sérsic function. It is part of the training sample presented in Gao & Ho (2017). Here we show the decomposition results that include all the above features (Model3 in their Table 6). Note that the uncertainties are different from those presented in their Table 6, since we include the model-induced uncertainties in this study.

NGC 6215: There are many foreground stars throughout the image. We model the disk break at $\sim 40''$. We mask the dust lanes on and around the bulge.

NGC 6221: The galaxy has a Seyfert 2 nucleus (Véron et al. 1981). We model the disk break at the edge of the spiral arms. An extra disk component is needed to account for the bar-like pattern produced by the spiral arms winding onto the bulge; otherwise, the bulge orientation will be incorrect. We mask the dust lanes on and around the bulge.

NGC 6300: The galaxy has a Seyfert 2 nucleus (Phillips et al. 1983), which was designated later as a changing-look AGN (Matt et al. 2003). We model the disk break at the bar radius but ignore the outer disk break at the edge of the spiral arms, treating it as an outer feature when estimating bulge errors. We mask the dust lanes around the bulge.

NGC 6392: The galaxy has a short and weak bar whose α and β have to be fixed. It has a two-disk configuration: an inner blue disk with spiral arms and an outer smooth red disk.

NGC 6492: The galaxy has a lens. We model the disk break at the edge of the spiral arms.

NGC 6673: The galaxy is classified as an elliptical in HyperLeda but as an S0 in RC3, and is recognized as a possible S0 in Huang et al. (2013a). It has a nuclear lens and an inner lens.

NGC 6684: The galaxy has a bar, an inner ring, and an outer ring/lens. A nuclear bar embedded in the bulge is roughly perpendicular to the large-scale bar.

NGC 6699: We model the broken disk with a Sérsic function.

NGC 6744: The galaxy has a LINER nucleus (Vaceli et al. 1997). We model the disk break at the bar radius but ignore the outer disk break at the edge of the spiral arms, treating it as an outer feature when estimating bulge errors. The galaxy is angularly so large that simultaneously solving the sky level during the fitting is impossible. So we fix the sky level to the value obtained via the direct approach. We mask the dust lanes around the bulge.

NGC 6753: The bulge is embedded in a nuclear lens and an inner lens.

NGC 6754: We model the disk break at the edge of the spiral arms. An extra disk component is needed to account for the bar-like pattern produced by the spiral arms winding onto the bulge, or else the bulge orientation and ellipticity will be incorrect. The disk is slightly lopsided. We mask the dust lanes around the bulge.

NGC 6782: The galaxy has a nuclear ring and a nuclear bar. We fix α and β of the bar component during the fitting. We model the disk break at the bar radius.

NGC 6788: The galaxy is well-described by a Sérsic bulge and an exponential disk, except for the central positive residuals of unknown physical nature.

NGC 6810: The galaxy has a distinctly blue nucleus with ambiguous classifications: Seyfert 2 nucleus (Kirhakos & Steiner 1990), H II nucleus (Véron-Cetty & Véron 1986; Strickland 2007; Brightman & Nandra 2008; Videla et al. 2013; Asmus et al. 2014), and H II/AGN composite nucleus (Brightman & Nandra 2011b; Yuan et al. 2010). This galaxy is actually edge-on, but its inclination angle is underestimated due to the presence of the thick disk. In addition, a lens-like component is found around the bulge. We mask the prominent dust lanes throughout the galaxy.

NGC 6814: The galaxy has a Seyfert 1.5 nucleus (Véron-Cetty & Véron 2010). We model the disk break at the bar radius.

NGC 6893: The galaxy has an inner lens and an outer lens. This galaxy was used in Gao & Ho (2017) to illustrate that the outer lenses/rings can be ignored for the purposes of bulge decomposition. Here we present the full details of its decomposition, with the outer lens included in the model.

NGC 6902: The bulge is surrounded by a ring/lens feature (Disk1 in Figure 2.282).

NGC 6907: The galaxy has a nuclear bar. We model the disk break at the edge of the spiral arms. The dust lanes near the bulge are masked.

NGC 6923: The galaxy has a short bar/lens. We model the disk break at the edge of the spiral arms. The dust lanes near the bulge are masked.

NGC 6935: The galaxy has a high- n bulge. We model the disk break at $\sim 20''$.

NGC 6942: The galaxy is barred and shows a disk break at $\sim 50''$. Spiral patterns are visible on the residual image, but they are quite weak and can be ignored.

NGC 6943: The galaxy has a weak bar. We model the disk break at $\sim 50''$.

NGC 7038: We model the disk break at the edge of spiral arms ($\sim 80''$).

NGC 7049: The galaxy has a lens. The circular dust lane around the bulge is masked during the fitting.

NGC 7059: We model the disk break at $\sim 50''$. The disk is slightly lopsided. We mask the dust lanes on and around the bulge.

NGC 7070: The galaxy has a distinctly blue nucleus of unknown nature and a flattened bulge. We model the broken disk with a Sérsic function. The disk is slightly lopsided.

NGC 7079: The galaxy has a bar and shows a disk break at $\sim 40''$.

NGC 7083: The disk has a Type II profile and bears three major spiral arms. It is part of the training sample presented in Gao & Ho (2017). Here we show the decomposition results that include all the above features (Model3

in their Table 5). Note that the uncertainties are different from those presented in their Table 5, since we include the model-induced uncertainties in this study.

NGC 7098: The galaxy probably has a nuclear ring. The bar is embedded in a lens/ring component.

NGC 7140: The galaxy has a nuclear ring. We model the disk break at the bar radius but ignore the outer disk break at the edge of the spiral arms, treating it as an outer feature when estimating bulge errors. We mask the dust lanes on and around the bulge and along the bar.

NGC 7144: The galaxy is classified as an elliptical in both HyperLeda and RC3, but is recognized as an S0 in [Huang et al. \(2013a\)](#). It has a nuclear lens and an inner lens.

NGC 7172: The galaxy is reported to host a Seyfert 2 nucleus ([Véron-Cetty & Véron 2010](#)), but we find no sign of the nucleus on the image, probably due to severe dust attenuation. We mask the prominent dust lane across the galaxy. We use two components to model the tidally distorted disk ([Turner et al. 1997](#)).

NGC 7192: The galaxy is classified as an elliptical in both HyperLeda and RC3, but is recognized as an S0 in [Huang et al. \(2013a\)](#). It has a nuclear lens and an inner lens.

NGC 7213: The galaxy has a Seyfert 1/LINER nucleus ([Phillips 1979](#); [Filippenko & Halpern 1984](#)) and a nuclear ring. We mask the dust lanes around the bulge. Significant sky gradient is present in the residuals.

NGC 7218: We model the disk break at $\sim 20''$. We strive to mask the dust lanes at the galaxy center. We find positive residuals of unknown physical nature at the center, probably due to mismatch between the best-fit model and the data caused by dust attenuation.

NGC 7314: The galaxy has a Seyfert 2 ([Asmus et al. 2014](#); [Koulouridis 2014](#)) or Seyfert 1 nucleus ([Véron-Cetty & Véron 1986, 2010](#)). We model the disk break at $\sim 60''$ and mask the dust lanes near the bulge.

NGC 7329: The galaxy has a prominent bulge and bar. The disk shows grand-design spiral arms that start from the inner ring. It is part of the training sample presented in [Gao & Ho \(2017\)](#). Here we show the decomposition results that include all the above features (Model3 in their Table 10). Note that the uncertainties are different from those presented in their Table 10, since we include the model-induced uncertainties in this study.

NGC 7371: The galaxy has a weak and short bar embedded in a lens/ring structure. We model the disk break at $\sim 30''$. We ignore the extra light of unknown physical nature in the galaxy outskirts ($\gtrsim 80''$) and treat it as an outer feature when estimating bulge errors.

NGC 7377: The galaxy has a nuclear lens and an inner lens. The dust lanes are masked during the fitting.

NGC 7392: The galaxy has a distinctly blue nucleus that was classified to be inactive ([Martini et al. 2003](#)). We fix α and β of the weak bar during the fitting. We model the disk break at the bar radius and at $\sim 70''$. We mask the spiral dust lanes approaching the center.

NGC 7412: We model the disk break at $\sim 40''$. An extra disk component is needed to account for the bar-like pattern produced by the spiral arms winding onto the bulge. We mask the circumnuclear dust lanes during the fitting.

NGC 7418: The galaxy hosts an NSC ([Böker et al. 2002](#)), a weak bulge, and a weak bar. We model the disk break at the edge of the spiral arms. The disk is slightly lopsided. We mask the dust lanes around the bulge.

NGC 7421: The galaxy has an NSC ([Georgiev & Böker 2014](#)). We model the disk break at the bar radius. The disk is significantly lopsided.

NGC 7424: The galaxy has an NSC ([Böker et al. 2002](#)). The blue and flattened bulge is embedded in a short and weak bar whose α and β are fixed during the fitting. We model the disk break at the bar radius but ignore the outer disk break at the edge of the spiral arms, treating it as an outer feature when estimating bulge errors. We mask the dust lanes on the bar.

NGC 7496: The galaxy has a distinctly blue nucleus with ambiguous classifications: star-forming nucleus ([Yuan et al. 2010](#)) and Seyfert 2 nucleus ([Véron-Cetty & Véron 2010](#)). We model the disk break at the bar radius but ignore the outer disk break at the edge of the spiral arms, treating it as an outer feature when estimating bulge errors. We mask the dust lanes on the bulge and along the bar.

NGC 7513: The galaxy has an NSC ([Carollo et al. 2002](#)). We fix α and β of the bar component, or else the bar will be unrealistically long. We model the disk break at the bar radius but ignore the outer disk break at the edge of the spiral arms, treating it as an outer feature when estimating bulge errors. We mask the dust lanes on the bulge and along the bar.

NGC 7531: The galaxy has a distinctly red nucleus that was classified to be Seyfert-like ([Véron-Cetty & Véron 1986](#)). We model both the inner lens and the outer lens. We mask the dust lane running through the bulge.

NGC 7552: The bulge is embedded in the bar and lens. We ignore the disk break at the edge of the spiral arms ($\sim 100''$) and treat it as an outer feature when estimating bulge errors.

NGC 7582: The galaxy is reported to host a Seyfert 2 nucleus (Véron-Cetty & Véron 2010), a star-forming nucleus (Yuan et al. 2010), or a composite nucleus (Véron-Cetty & Véron 1986). However, we find no sign of a nucleus on the image, and attempts to include a PSF component in the fit fails. The bar is embedded in a lens. We fix α and β of the bar component, or else the bar will be unrealistically long. We model the disk break at the edge of the spiral arms.

NGC 7590: The galaxy is reported to host a Seyfert 2 nucleus (Véron-Cetty & Véron 2010). We find no sign of the nucleus on the image. Forcibly including a PSF component does not impact the bulge parameters much, and we simply ignore the purported nucleus. We model the disk break at the edge of the spiral arms. We mask the dust lanes on and near the bulge.

NGC 7606: We model the disk break at the edge of spiral arms.

NGC 7689: We model the disk break at the edge of spiral arms.

NGC 7723: We model the disk break at the bar radius but ignore the outer disk break at the edge of the spiral arms ($\sim 80''$), treating it as an outer feature when estimating bulge errors. We mask the dust lanes along the bar.

NGC 7755: The galaxy has a nuclear ring. We model the disk break at the bar radius but ignore the outer disk break at the edge of the spiral arms, treating it as an outer feature when estimating bulge errors. We mask the circumnuclear dust lanes.

REFERENCES

- Alonso-Herrero, A., Pereira-Santaella, M., Rieke, G. H., & Rigopoulou, D. 2012, *ApJ*, 744, 2
- Andredakis, Y. C., Peletier, R. F., & Balcells, M. 1995, *MNRAS*, 275, 874
- Andredakis, Y. C., & Sanders, R. H. 1994, *MNRAS*, 267, 283
- Asmus, D., Hönig, S. F., Gandhi, P., Smette, A., & Duschl, W. J. 2014, *MNRAS*, 439, 1648
- Athanassoula, E. 2005, *MNRAS*, 358, 1477
- Barth, A. J., Filippenko, A. V., & Moran, E. C. 1999, *ApJ*, 525, 673
- Binney, J., & Tremaine, S. 1987, *Galactic Dynamics* (Princeton, NJ: Princeton Univ. Press)
- Böker, T., Laine, S., van der Marel, R. P., et al. 2002, *AJ*, 123, 1389
- Bournaud, F. 2016, in *Galactic Bulges*, ed. E. Laurikainen, R. Peletier, & D. Gadotti (New York: Springer), 355
- Brightman, M., & Nandra, K. 2008, *MNRAS*, 390, 1241
- Brightman, M., & Nandra, K. 2011a, *MNRAS*, 413, 1206
- Brightman, M., & Nandra, K. 2011b, *MNRAS*, 414, 3084
- Burstein, D. 1979, *ApJ*, 234, 435
- Byun, Y.-I. 1992, PhD thesis, Australian National Univ.
- Byun, Y. I., & Freeman, K. C. 1995, *ApJ*, 448, 563
- Capaccioli, M., Held, E. V., & Nieto, J.-L. 1987, *AJ*, 94, 1519
- Carollo, C. M., Stiavelli, M., de Zeeuw, P. T., & Mack, J. 1997, *AJ*, 114, 2366
- Carollo, C. M., Stiavelli, M., Seigar, M., de Zeeuw, P. T., & Dejonghe, H. 2002, *AJ*, 123, 159
- Ciotti, L. 1991, *A&A*, 249, 99
- Cisternas, M., Gadotti, D. A., Knapen, J. H., et al. 2013, *ApJ*, 776, 50
- da Silva, P., Steiner, J. E., & Menezes, R. B. 2017, *MNRAS*, 470, 3850
- D'Agostino, J. J., Poetrodjojo, H., Ho, I.-T., et al. 2018, *MNRAS*, 479, 4907
- de Jong, R. S. 1996a, *A&AS*, 118, 557
- de Jong, R. S. 1996b, *A&A*, 313, 45
- de Vaucouleurs, G., de Vaucouleurs, A., Corwin, Jr., H. G., et al. 1991, *Third Reference Catalog of Bright Galaxies* (New York: Springer)
- Decarli, R., Gavazzi, G., Arosio, I., et al. 2007, *MNRAS*, 381, 136
- Desroches, L.-B., & Ho, L. C. 2009, *ApJ*, 690, 267
- Eggen, O. J., Lynden-Bell, D., & Sandage, A. R. 1962, *ApJ*, 136, 748
- Erwin, P., Beckman, J. E., & Pohlen, M. 2005, *ApJL*, 626, L81
- Erwin, P., Pohlen, M., & Beckman, J. E. 2008, *AJ*, 135, 20
- Faber, S. M. 1977, in *Evolution of Galaxies and Stellar Populations*, ed. B. M. Tinsley & R. B. Larson (New Haven, CT: Yale Univ. Obs.), 157
- Filippenko, A. V., & Halpern, J. P. 1984, *ApJ*, 285, 458
- Fisher, D. B., & Drory, N. 2008, *AJ*, 136, 773
- Fisher, D. B., & Drory, N. 2011, *ApJL*, 733, L47
- Fisher, D. B., Drory, N., & Fabricius, M. H. 2009, *ApJ*, 697, 630
- Foord, A., Gallo, E., Hodges-Klück, E., et al. 2017, *ApJ*, 841, 51
- Freeman, K. C. 1970, *ApJ*, 160, 811
- Gao, H., & Ho, L. C. 2017, *ApJ*, 845, 114

- Gao, H., Ho, L. C., Barth, A. J., & Li, Z.-Y. 2018, *ApJ*, 862, 100
- Gavazzi, G., Consolandi, G., Dotti, M., et al. 2013, *A&A*, 558, A68
- Georgiev, I. Y., & Böker, T. 2014, *MNRAS*, 441, 3570
- Giuricin, G., Tamburini, L., Mardirossian, F., Mezzetti, M., & Monaco, P. 1994, *ApJ*, 427, 202
- Gott, III, J. R. 1977, *ARA&A*, 15, 235
- Graham, A. W. 2001, *AJ*, 121, 820
- Graham, A. W., & Worley, C. C. 2008, *MNRAS*, 388, 1708
- Greenhill, L. J., Ellingsen, S. P., Norris, R. P., et al. 2002, *ApJ*, 565, 836
- Grier, C. J., Mathur, S., Ghosh, H., & Ferrarese, L. 2011, *ApJ*, 731, 60
- Grosbøl, P., Patsis, P. A., & Pompei, E. 2004, *A&A*, 423, 849
- Hau, G. K. T., Bower, R. G., Kilborn, V., et al. 2008, *MNRAS*, 385, 1965
- Héraudeau, P., & Simien, F. 1995, *ApL&C*, 31, 219
- Ho, L. C. 2009, *ApJ*, 699, 626
- Ho, L. C., Filippenko, A. V., & Sargent, W. L. W. 1997, *ApJS*, 112, 315
- Ho, L. C., Li, Z.-Y., Barth, A. J., Seigar, M. S., & Peng, C. Y. 2011, *ApJS*, 197, 21
- Huang, S., Ho, L. C., Peng, C. Y., Li, Z.-Y., & Barth, A. J. 2013a, *ApJ*, 766, 47
- Huang, S., Ho, L. C., Peng, C. Y., Li, Z.-Y., & Barth, A. J. 2013b, *ApJL*, 768, L28
- Huang, S., Ho, L. C., Peng, C. Y., Li, Z.-Y., & Barth, A. J. 2016, *ApJ*, 821, 114
- Hubble, E. P. 1926, *ApJ*, 64, 321
- Hubble, E. P. 1936, *Realm of the Nebulae* (New Haven, CT: Yale Univ. Press)
- Hunt, L. K., & Malkan, M. A. 2004, *ApJ*, 616, 707
- Kent, S. M. 1985, *ApJS*, 59, 115
- Kent, S. M. 1986, *AJ*, 91, 1301
- Khosroshahi, H. G., Wadadekar, Y., & Kembhavi, A. 2000, *ApJ*, 533, 162
- Kim, T., Gadotti, D. A., Athanassoula, E., et al. 2016, *MNRAS*, 462, 3430
- Kim, T., Gadotti, D. A., Sheth, K., et al. 2014, *ApJ*, 782, 64
- Kirhakos, S. D., & Steiner, J. E. 1990, *AJ*, 99, 1722
- Kodaira, K., Watanabe, M., & Okamura, S. 1986, *ApJS*, 62, 703
- Kormendy, J. 1977a, *ApJ*, 217, 406
- Kormendy, J. 1977b, *ApJ*, 218, 333
- Kormendy, J., Drory, N., Bender, R., & Cornell, M. E. 2010, *ApJ*, 723, 54
- Kormendy, J., & Ho, L. C. 2013, *ARA&A*, 51, 511
- Kormendy, J., & Kennicutt, Jr., R. C. 2004, *ARA&A*, 42, 603
- Koulouridis, E. 2014, *A&A*, 570, A72
- Laurikainen, E., Peletier, R., & Gadotti, D. 2016, *Galactic Bulges* (New York: Springer)
- Laurikainen, E., Salo, H., & Buta, R. 2005, *MNRAS*, 362, 1319
- Laurikainen, E., Salo, H., Buta, R., & Knapen, J. H. 2007, *MNRAS*, 381, 401
- Laurikainen, E., Salo, H., Buta, R., Knapen, J. H., & Comerón, S. 2010, *MNRAS*, 405, 1089
- Li, Z.-Y., Ho, L. C., & Barth, A. J. 2017, *ApJ*, 845, 87
- Li, Z.-Y., Ho, L. C., Barth, A. J., & Peng, C. Y. 2011, *ApJS*, 197, 22
- Maiolino, R., Ruiz, M., Rieke, G. H., & Papadopoulos, P. 1997, *ApJ*, 485, 552
- Maiolino, R., Comastri, A., Gilli, R., et al. 2003, *MNRAS*, 344, L59
- Martini, P., Regan, M. W., Mulchaey, J. S., & Pogge, R. W. 2003, *ApJS*, 146, 353
- Matt, G., Guainazzi, M., & Maiolino, R. 2003, *MNRAS*, 342, 422
- Meert, A., Vikram, V., & Bernardi, M. 2015, *MNRAS*, 446, 3943
- Méndez-Abreu, J., Ruiz-Lara, T., Sánchez-Menguiano, L., et al. 2017, *A&A*, 598, A32
- Meurer, G. R., Hanish, D. J., Ferguson, H. C., et al. 2006, *ApJS*, 165, 307
- Möllenhoff, C. 2004, *A&A*, 415, 63
- Möllenhoff, C., & Heidt, J. 2001, *A&A*, 368, 16
- Oohama, N., Okamura, S., Fukugita, M., Yasuda, N., & Nakamura, O. 2009, *ApJ*, 705, 245
- Paturel, G., Petit, C., Prugniel, P., et al. 2003, *A&A*, 412, 45
- Peng, C. Y., Ho, L. C., Impey, C. D., & Rix, H.-W. 2002, *AJ*, 124, 266
- Peng, C. Y., Ho, L. C., Impey, C. D., & Rix, H.-W. 2010, *AJ*, 139, 2097
- Phillips, M. M. 1979, *ApJL*, 227, L121
- Phillips, M. M., Charles, P. A., & Baldwin, J. A. 1983, *ApJ*, 266, 485
- Pohlen, M., & Trujillo, I. 2006, *A&A*, 454, 759
- Renzini, A. 1999, in *The Formation of Galactic Bulges*, ed. C. M. Carollo, H. C. Ferguson, & R. F. G. Wyse (Cambridge: Cambridge Univ. Press), 9
- Rush, B., Malkan, M. A., & Spinoglio, L. 1993, *ApJS*, 89, 1
- Salo, H., Laurikainen, E., Laine, J., et al. 2015, *ApJS*, 219, 4
- Sandage, A. 1961, *The Hubble Atlas of Galaxies* (Washington, DC: Carnegie Institution of Washington)
- Scorza, C., & Bender, R. 1990, *A&A*, 235, 49

- Sellwood, J. A. 2014, *RvMP*, 86, 1
- Sérsic, J. L. 1968, *Atlas de Galaxias Australes* (Córdoba: Obs. Astron., Univ. Nac. Córdoba)
- Seth, A., Agüeros, M., Lee, D., & Basu-Zych, A. 2008, *ApJ*, 678, 116
- Seyfert, C. K. 1943, *ApJ*, 97, 28
- Shaw, M. A., & Gilmore, G. 1989, *MNRAS*, 237, 903
- She, R., Ho, L. C., & Feng, H. 2017a, *ApJ*, 835, 223
- She, R., Ho, L. C., & Feng, H. 2017b, *ApJ*, 842, 131
- Sheth, K., Regan, M., Hinz, J. L., et al. 2010, *PASP*, 122, 1397
- Shields, J. C., Walcher, C. J., Böker, T., et al. 2008, *ApJ*, 682, 104
- Siebenmorgen, R., Haas, M., Pantin, E., et al. 2008, *A&A*, 488, 83
- Simard, L., Mendel, J. T., Patton, D. R., Ellison, S. L., & McConnell, A. W. 2011, *ApJS*, 196, 11
- Simien, F., & de Vaucouleurs, G. 1986, *ApJ*, 302, 564
- Simien, F., & Michard, R. 1990, *A&A*, 227, 11
- Smith, L. J., Crowther, P. A., Calzetti, D., & Sidoli, F. 2016, *ApJ*, 823, 38
- Solanes, J. M., Salvador-Sole, E., & Sanroma, M. 1989, *AJ*, 98, 798
- Sosa-Brito, R. M., Tacconi-Garman, L. E., Lehnert, M. D., & Gallimore, J. F. 2001, *ApJS*, 136, 61
- Strickland, D. K. 2007, *MNRAS*, 376, 523
- Tonini, C., Mutch, S. J., Croton, D. J., & Wyithe, J. S. B. 2016, *MNRAS*, 459, 4109
- Toomre, A. 1977, in *Evolution of Galaxies and Stellar Populations*, ed. B. M. Tinsley & R. B. Larson (New Haven, CT: Yale Univ. Obs.), 401
- Turner, T. J., George, I. M., Nandra, K., & Mushotzky, R. F. 1997, *ApJS*, 113, 23
- Vaceli, M. S., Viegas, S. M., Gruenwald, R., & de Souza, R. E. 1997, *AJ*, 114, 1345
- Véron, M. P., Véron, P., & Zuiderwijk, E. J. 1981, *A&A*, 98, 34
- Véron-Cetty, M.-P., & Véron, P. 1986, *A&AS*, 66, 335
- Véron-Cetty, M.-P., & Véron, P. 2010, *A&A*, 518, A10
- Videla, L., Lira, P., Andrews, H., et al. 2013, *ApJS*, 204, 23
- Weinzirl, T., Jogee, S., Khochfar, S., Burkert, A., & Kormendy, J. 2009, *ApJ*, 696, 411
- Wyse, R. F. G., Gilmore, G., & Franx, M. 1997, *ARA&A*, 35, 637
- Yu, S.-Y., & Ho, L. C. 2018a, *ApJ*, 869, 29
- Yu, S.-Y., & Ho, L. C. 2018b, *ApJ*, in press, arXiv:1812.06010
- Yuan, T.-T., Kewley, L. J., & Sanders, D. B. 2010, *ApJ*, 709, 884
- Zhang, W. M., Soria, R., Zhang, S. N., Swartz, D. A., & Liu, J. F. 2009, *ApJ*, 699, 281